Chapter 5

Conjugate Hard X-ray Footpoints — Unshearing Motions, Correlations, and Asymmetries: The 2003-10-29 X10 Flare[1]

5.1 Introduction

As noted in §1, magnetic reconnection is believed to be the primary channel of energy release, which leads to heating of plasma and acceleration of particles in solar flares. Details of reconnection and particle acceleration, however, remain largely unknown. X-ray observations of the loop-top (LT) and footpoint (FP) sources, particularly of their spatial, temporal, and spectral properties, combined with magnetic field measurements of the flare region, can provide critical information about how and where electrons are accelerated subsequent to magnetic reconnection. In Chapter 4 we focused on emission from coronal sources, while here we turn our attention to emission from conjugate FPs.

Unshearing and/or approaching motions of double Hα kernels and/or HXR FPs were recently found in the early impulsive peaks of three flares (Ji et al., 2004, 2006, 2007). These FP motions occurred during the period when the LT source descended in altitude, similar to that reported by Sui & Holman (2003), Sui et al. (2004), and Liu, W. et al. (2004a, 2008b).The approach of FPs was also evident in two of the four events reported by Fletcher & Hudson (2002). These new observations challenge the above classical picture. Veronig et al. (2006) proposed a collapsing magnetic trap model to explain the LT descending motions, which, however, cannot explain the FP approaching motions. Ji et al. (2007) suggested that such correlated FP and LT motions result from relaxation of flare loops. The reported LT descents were usually observed in flares occurring near the solar limb where the LT height can be readily measured, but the FP motions in the east-west direction are obscured by projection effects. Flares close to disk center, like the one reported here, can give an alternative perspective.

[1]The majority of this chapter was submitted to ApJ for publication (Liu, W. et al., 2008a).

Correlations between a pair of conjugate HXR FPs are expected, since they are believed to be produced by high-energy electrons released from the same acceleration region. The relative timing of conjugate FPs was found to be simultaneous within an uncertainty of 0.1–0.3 s (Sakao, 1994) based on *Yohkoh* Hard X-Ray Telescope (HXT) *Yohkoh* observations. For double FPs in tens of flares observed by the *Ramaty High Energy Solar Spectroscopic Imager* (*RHESSI*), temporal correlations in the HXR fluxes in two wide energy bands (25–50 and 50–100 keV) with a time resolution of 8 s were identified by Jin & Ding (2007). Spectral correlations at individual HXR peaks were investigated by Saint-Hilaire et al. (2008), who found power-law indexes that differed by <0.6. This spectral index difference is similar to that found by Sakao (1994), but smaller than the values as high as 1 or 2 reported by Petrosian et al. (2002) based on analysis of *Yohkoh* HXT images.

Asymmetric FPs, i.e., conjugate FPs with different properties (HXR fluxes, magnetic field strengths, etc.) are commonly observed (e.g., Sakao, 1994). This has been ascribed to asymmetric magnetic mirroring where a brighter HXR FP is associated with a weaker magnetic field (Li et al., 1997; Aschwanden et al., 1999; Qiu et al., 2001; Li & Ding, 2004). This picture is consistent with observations at radio wavelengths where brighter microwave emission appears at the FP with the stronger magnetic field (e.g., Kundu et al., 1995; Wang et al., 1995). Exceptions to the mirroring scenario were reported by Goff et al. (2004), who found one third of 32 *Yohkoh* flares with an opposite trend, that is, the association of the brighter HXR FP with the stronger magnetic field. Falewicz & Siarkowski (2007) re-examined three exceptions in the sample of Goff et al. and attributed this opposite asymmetry to different column densities in the two legs of the flare loop, as also suggested by Emslie et al. (2003) and Liu, W. (2006). Temporal variations of the flux asymmetry were found in a *Yohkoh* flare (Siarkowski & Falewicz, 2004), and energy- and time-dependent variations were seen in a *RHESSI* flare (Alexander & Metcalf, 2002). The latter were interpreted by McClements & Alexander (2005) as a consequence of an asymmetric, energy-dependent and time-dependent injection of accelerated electrons.

Previous studies of conjugate HXR FPs, in general, suffered from limited time, spatial, and/or energy resolution and/or coverage of HXR emission, mainly restricted by the instrumental capabilities, or from lack of magnetic field measurements. We report here on a comprehensive study of the conjugate FPs in the 2003 October 29 X10 flare observed by *RHESSI* that overcomes many of the previous shortcomings. This flare provides a unique opportunity to track the spatial and spectral evolution of the double HXR FPs and their associated magnetic fields in great detail, and to study all three interrelated aspects: *unshearing motions*, *correlations*, and *asymmetries*. This flare occurred near disk center, where FP motions and line-of-sight magnetic field measurements have minimum projection effects. Its long ($\sim$20 minutes) impulsive phase and high *RHESSI* count rates up to several hundred keV allow for a detailed study of variations both in time and energy. The flare was also well observed by the *Transition Region and Coronal Explorer* (*TRACE*), the *Solar and Heliospheric Observatory* (*SOHO*), and other spacecraft and many ground-based observatories. The rich database of multiwavelength observations and a wide range of literature covering different aspects of this event (e.g., Xu et al., 2004; Krucker et al., 2005) are particularly beneficial for this in-depth study.

We present the observations and data analysis in §5.2. These include general *RHESSI* light curves and images, *RHESSI* imaging spectroscopy, and multiwavelength observations.

We investigate in §5.3 the two phases (fast and slow) of unshearing motions of the FPs and the associated LT motion. In §5.4 we explore various correlations of the FPs, particularly of their HXR fluxes, spectral shapes, spatial variations, and magnetic fields. Possible contributions to the HXR flux and spectral asymmetries are discussed in §5.5, followed by our summary in §5.6. A discussion of pulse pileup effects, technical details on coaligning images made by different instruments, a mathematical treatment of the asymmetric column density effect, and an estimate of the coronal column densities in the legs of the flare loop are given in Appendixes A.4.2, B.1, B.2, and B.3, respectively.

5.2 Observations and Data Analysis

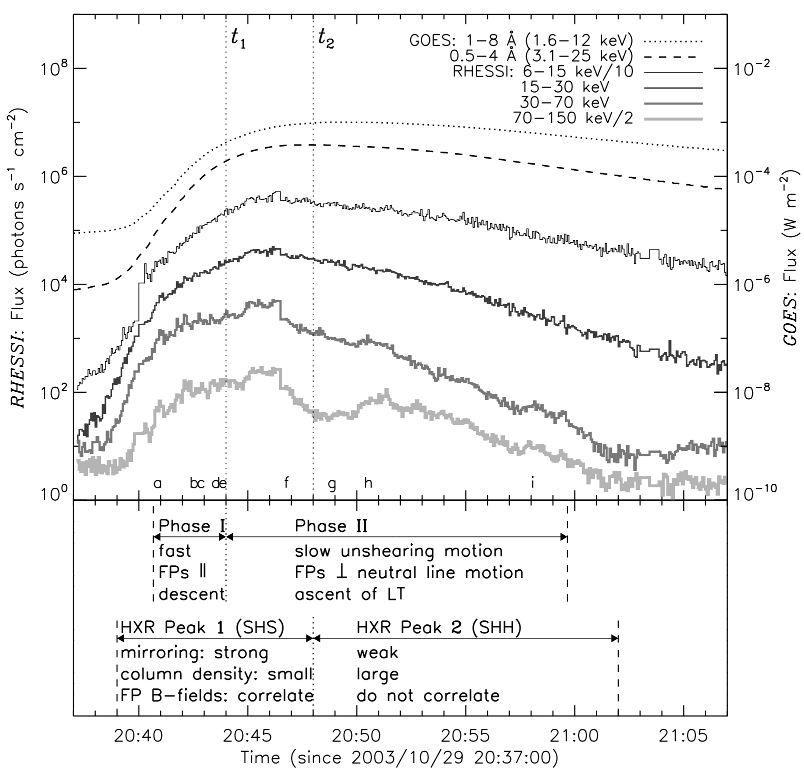

Figure 5.1: *RHESSI* and *GOES*-12 light curves of the 2003 October 29 X10 flare. The *RHESSI* fluxes (*left scale*) were obtained by spatially integrating the images of the flare region reconstructed for every consecutive 4 s interval (from Ji et al. 2008). The 6–15 and 70–150 keV curves are scaled down by factors of 10 and 2, respectively. The two channel *GOES* fluxes are on the right scale. The vertical dotted lines mark the two transitions (t_1 and t_2) denoted in the bottom panel. t_1 divides Phases I and II based on FP motions (see §5.3), and t_2 divides >70 keV HXR Peaks 1 and 2 (see §5.4.1). The letters "*a–i*" on the middle x-axis indicate the times of the nine images shown in Fig. 5.2. Note that both attenuators were in place (A3 state) during the time range shown here, except before 20:40 UT and during the interval of 21:03:12–21:03:40 UT, when only the thin attenuators were in (A1 state). The changes of the attenuator state were responsible for the artificial jumps of the light curves at these times. Another jump occurred at 20:46:36 UT when the front detector changed its decimation state from FD1 to FD4 (Smith et al., 2002) [from Liu, W. et al. 2008a].

We present in this section general multiwavelength and *RHESSI* X-ray observations to indicate the context for our detailed discussions to follow on the conjugate FPs. The event under study occurred in AR 10486 (W5°S18°) starting at 20:37 UT on 2003 October 29, during the so-called Halloween storms (e.g., Gopalswamy et al., 2005). It was a *Geostationary Operational Environment Satellite* (*GOES*) X10 class, white-light, two-ribbon flare, which produced strong gamma-ray line emission (Hurford et al., 2006) and helioseismic signals (Donea & Lindsey, 2005). It was associated with various other solar activity, including a fast ($\sim$2000 $\mathrm{km\,s^{-1}}$) halo coronal mass ejections (CMEs), and heliospheric consequences. This was the first white-light flare observed at the opacity minimum at 1.6 μm, which corresponds to the deepest layer of the photosphere that can be seen (Xu et al., 2004, 2006). There were strong photospheric shearing flows present near the magnetic neutral lines in this active region prior to the flare onset (Yang et al., 2004), which may be related to the unusually large amount of magnetic free energy ($\sim$6 $\times 10^{33}$ ergs; Metcalf et al. 2005) stored in this AR. By analyzing Huairou and Mees vector magnetograms, Liu et al. (2007) proposed that this flare resulted from reconnection between magnetic flux tubes having opposite current helicities. This may be connected to the soft X-ray sigmoid structure and unshearing motions of HXR FPs found by Ji et al. (2008) during the early phase of the flare. Liu & Hayashi (2006), using potential field extrapolations from the *SOHO* Michelson Doppler Imager (MDI) observations, investigated the large-scale coronal magnetic filed of AR 10486 and its high productivity of CMEs. Liu et al. (2006a) found remote brightenings more than 2×10^5 km away from the main flare site. Solar energetic particles (SEPs) were detected after this flare by *GOES* and the *Advanced Composition Explorer* (*ACE*).

Our goal in this chapter is to understand the temporal and spectral variations of the asymmetric HXR FPs and their associated magnetic fields. We thus focus on HXR observations obtained by *RHESSI* and line-of-sight photospheric magnetograms obtained by *SOHO* MDI. Vector magnetograms measured with chromospheric emission lines are more desirable for this study, as relevant magnetic mirroring may take place above the chromosphere where thick-target HXRs are produced. However, the extensive efforts required for calibrating vector magnetograms are not warranted for this study because of possibly small improvements that will not alter our conclusions. Specifically, because this flare is close to disk center (W5°S18°), line-of-sight MDI magnetograms already provide a good approximation (within 5%) of the vertical component of the photospheric magnetic field that is assumed to be proportional to the total chromospheric magnetic field strength. It would have been interesting to examine microwave images which may show opposite FP asymmetry as in HXRs (Kundu et al., 1995). However, spectrograms of this flare obtained at the Owens Valley Solar Array do not allow for image reconstruction due to poor data quality (J. Lee & C. Liu, private communication), while Nobeyama was not observing (before 6 AM, local time).

5.2.1 *RHESSI* Light Curves and Images

RHESSI had very good coverage of this event. However, HXR counts, particularly at high energies, were heavily contaminated by particles from the Earth's radiation belts during the course of the flare. Fortunately, count rates produced by these particles are unmodulated and are removed during image reconstruction (Hurford et al., 2002). Therefore, CLEAN images were made at short time intervals for each energy bin and then spatially integrated to obtain a light curve. Such *RHESSI* light curves, as shown in Figure 5.1a together with *GOES* fluxes, were obtained by Ji et al. (2008) by integrating consecutive 4 s images. We find that, at low energies (<30 keV), the X-ray light curves show a single peak and an almost exponential decay after the maximum. At high energies (>70 keV), there are two peaks (Peaks 1 and 2) divided at 20:48 UT.

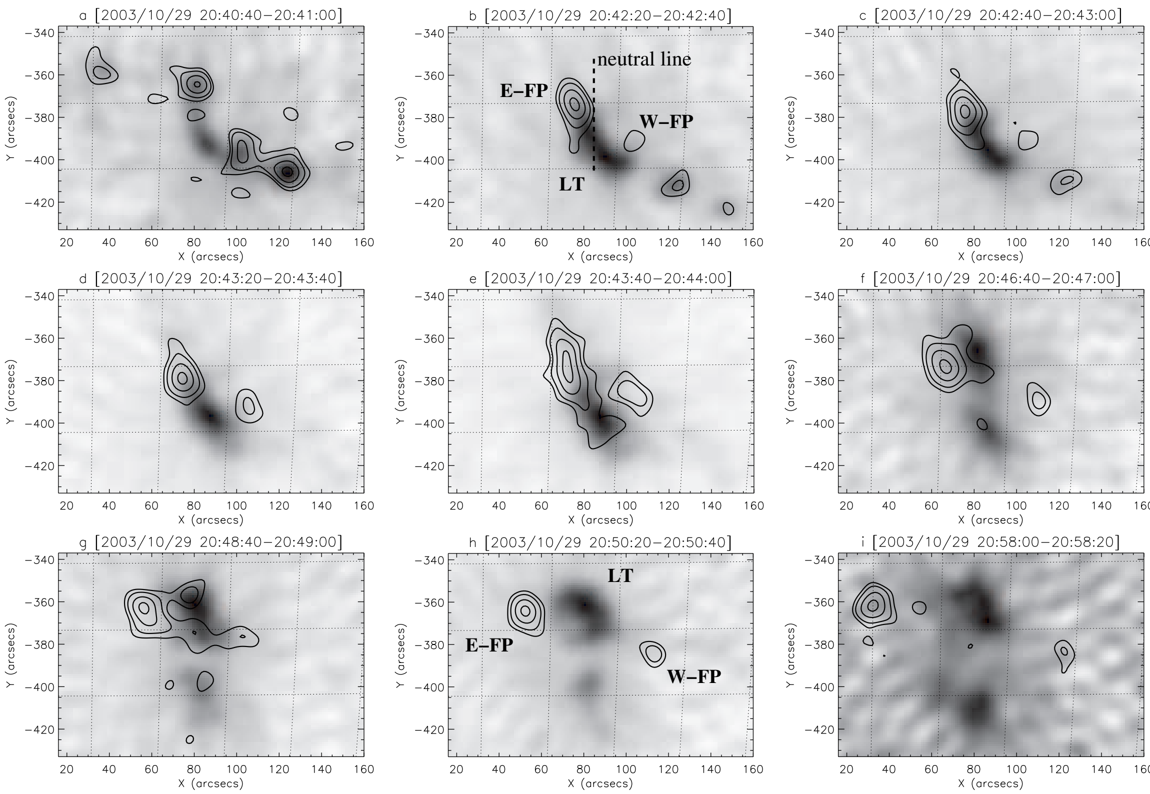

Figure 5.2: Evolution of HXR sources as seen in *RHESSI* CLEAN images made with detectors 3–8 (FWHM resolution 9.8″) in two energy bands, 12–25 keV as gray scale and 60–100 keV as contours (at 23%, 35%, 60%, and 90% of the maximum of each image). The dashed line in panel b shows the location of the magnetic neutral line shown in Fig. 5.6a that has been corrected for the solar rotation to the time of this image. The dotted lines mark the heliographic longitudes and latitudes with 2° spacing [from Liu, W. et al. 2008a].

To obtain the flare morphology and its general evolution, we focused on a time range from 20:40:40 to 20:59:40 UT beyond which the double conjugate FPs of interest (identified below) were not clearly imaged, due to complex morphology and/or low count rates. We first divided this time range into 57 consecutive 20 s intervals, except for one interval that was shortened to 12 s to avoid the decimation state change at 20:46:36 UT. We then reconstructed images in two broad energy bands, 12–25 and 60-100 keV, using the CLEAN algorithm and uniform weighting among detectors 3–8 (Hurford et al., 2002). The effective FWHM angular resolution is 9.8″.

A sample of the resulting images is shown in Figure 5.2. Early in the flare (before

20:43:20 UT, Fig. 5.2*d*), several bright points at 60–100 keV are dispersed across the image, suggesting FPs of multiple loops. Part of the 12–25 keV emission appears elongated and curved between the adjacent FPs, corresponding to the LT source(s). Toward the south-west, part of the 12–25 keV emission seems to overlap with the FP emission, possibly due to either a projection effect. As time proceeds, the FP structure seen at 60–100 keV becomes simpler, and only two distinct FPs are present (after 20:43:20 UT). They generally move away from each other. At the same time, the 12–25 keV emission gradually changes from one to two LT sources, one in the north and the other in the south.

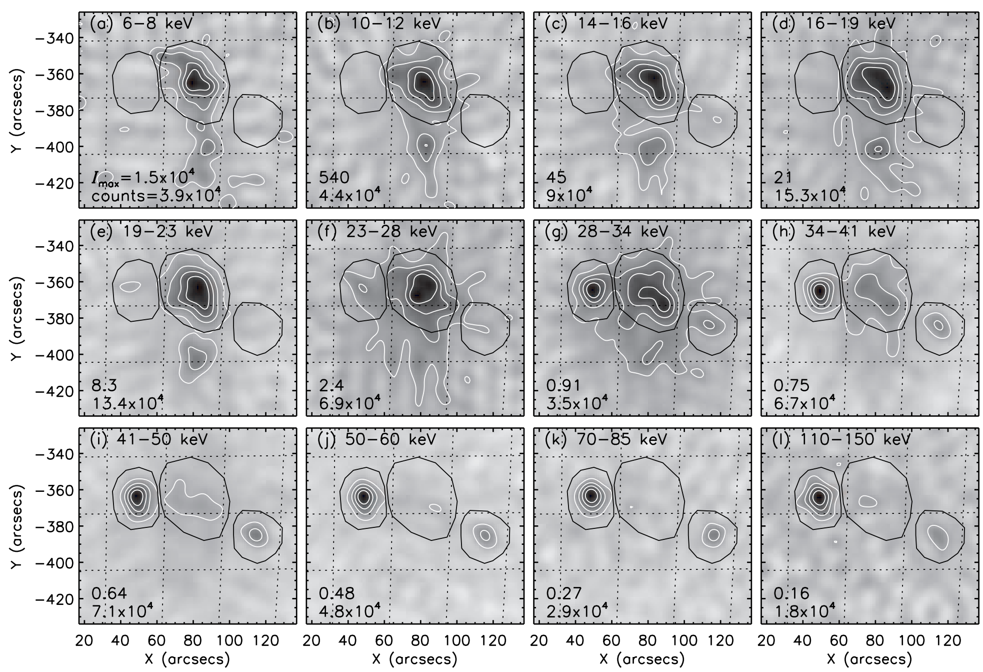

Figure 5.3: CLEAN images in different energy bins at 20:51:20–20:51:40 UT made with detectors 3–9. The contour levels are 20%, 40%, 60%, and 80% of the maximum surface brightness, $I_{\max}$ (shown in the lower left corner of each panel, in units of photons $\mathrm{cm}^{-2}\,\mathrm{s}^{-1}\,\mathrm{arcsec}^{-2}$), of each individual image. The number below $I_{\max}$ indicates the total counts accumulated by the detectors used. The heliographic grid spacing is 2°. The same three dark, hand-drawn polygons in each panel were used to obtain the fluxes of the LT and two FP sources [from Liu, W. et al. 2008a].

We identified the conjugate FPs and the corresponding LT source of interest as follows for detailed analysis: (1) At later times (after 20:43:20 UT), only two FPs are seen in each image at 60-100 keV and so they are considered conjugate. We call the FP on the eastern (left) side E-FP and the one on the western (right) side W-FP (see, e.g., Fig. 5.2*h*). (2) At earlier times when more than two FPs are present, we set forth the following selection criteria: (*a*) The source morphology of the two conjugate FPs must be consistent with the picture that they are magnetically connected through the LT source between them seen in the corresponding 12–25 keV image (see, e.g., Fig. 5.2*b*). (*b*) During the time evolution the two FPs must show continuity and consistency in position and HXR flux, which other short-lived FPs lack. Under these criteria, the selected E-FP is the brightest FP to the east of the magnetic neutral line (*thick dashed* in Figs. 5.2*b* and 5.6*a*), and W-FP is the one to the west located nearest to the neutral line. (3) Once the conjugate FPs are found, their corresponding LT source was identified as the 12–25 keV emission that lies closest to the straight line joining the FPs. For example, at later times (see, e.g., Fig. 5.2*h*), the northern LT is selected, while the southern LT is ignored since it does not seem to have any corresponding FP emission, presumably because of its faintness that exceeds *RHESSI*'s dynamic range ($\gtrsim$10:1 for images, Hurford et al., 2002, see Appendix §A.5).

5.2.2 Imaging Spectroscopy of Footpoint and Loop-top Sources

Next, we examine the spectroscopic characteristics of the LT and FP sources and their temporal evolution. For each of the 57 consecutive 20 s intervals defined above, we reconstructed CLEAN images in 16 energy bins that are progressively wider from 6 to 150 keV. A sample of these images is shown in Figure 5.3 for 20:51:20–20:51:40 UT, where four images showing similar morphology as in neighboring energy bins are omitted. The emission is dominated by the two LT sources at low energies and the double FP sources at high energies.

The next step was to obtain photon fluxes of the sources for each time interval. For each FP source, we used a hand-drawn polygon that envelops all the 10% (of the maximum brightness of the image) contours at energies where this FP source was clearly imaged. For the corresponding LT source, we drew a polygon that encloses the 20% contours, which was selected to minimize spatial contamination from the FPs. We then read the resulting multiple-energy image cube into the standard *RHESSI* spectral analysis software (OSPEX) package. This package integrates photon fluxes inside each polygon, and uses the full detector response matrix to estimate the true incident photon spectrum. The RMS of the residual map of the CLEAN image was used to calculate the uncertainty for the photon flux in each energy bin, with proper consideration of the source area and grid spatial resolution. This imaging spectroscopy technique is detailed by Liu, W. et al. (2008b). Note that we did not use contours at a fixed level (as opposed to polygons fixed in space) to obtain the fluxes because of the complex source morphology that makes such contours vary with energy.

One important issue for this X10 flare is pulse pileup (Smith et al., 2002) that at high count rates distorts the count-rate spectrum. We have discussed in Appendix A.4.2 various effects of pileup on our analysis and the remedy that we have applied to minimize them. Although it is currently not possible to obtain accurate spectra throughout the full energy range for all sources, pileup mainly affects the LT sources in the energy range of 20–50 keV (e.g., see Figs. 5.3*h* and 5.3*k*). In other words, pileup effects are negligible for the LT sources below 20 keV and for the FP sources above 50 keV. This conclusion enabled us to confine the extent of pileup effects both in energy and in space, and yet to infer desired spectral information. We thus fitted the LT spectrum below 20 keV with an assumed isothermal model from CHIANTI ver. 5.2 (Young et al., 2003), using the coronal iron abundance of 4 times the photospheric value, to determine its temperature (T) and emission measure (EM); we fitted the FP spectrum above 50 keV with an assumed single power-law model to find its spectral index (γ) and normalization flux (I) at the reference energy of 50 keV.

Spectra of the LT and FP sources are shown in Figure 5.4*a* for the interval of 20:44:40–20:45:00 UT (during the main impulsive peak). Above 50 keV, both FP spectra have a power-law shape, with the E-FP flux being twice that of W-FP but only slightly harder. Consequently, the W-to-E ratio of the two FP spectra generally decreases with energy

(Fig. 5.4*b*) or stays constant within uncertainties. Below 20 keV the LT spectrum shows the exponential shape of isothermal bremsstrahlung emission, with the iron line feature at 6.7 keV visible. Note that below 50 keV the FP spectra may be compromised by pileup effects[2] and spatial contamination from the LT source, and likewise above 20 keV the apparent LT flux is contaminated by FP emission at the same energy and by pileup from lower energies (Fig. 5.4*a*).

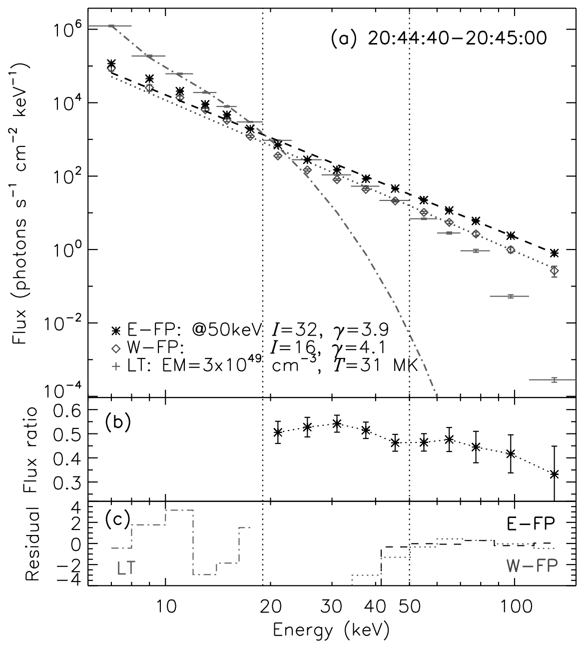

Figure 5.4: (*a*) Spatially resolved spectra of the LT and two FP sources at 20:44:40–20:45:00 UT. The horizontal bars on the LT spectrum represent the energy bin widths in the range of 6–150 keV. The dashed and dotted lines are power-law fits from 50–150 keV for E-FP and W-FP, respectively, and the dot-dashed line is a single temperature thermal fit from 6–19 keV for the LT. The legend shows the photon fluxes (I) at 50 keV and the spectral indexes (γ) for the FPs, and the emission measure (EM) and temperature (T) for the LT. (*b*) Ratio of the W-to-E FP fluxes. (*c*) Fitting residuals normalized by the 1σ uncertainties for the LT (*dot-dashed*), E-FP (*dashed*) and W-FP (*dotted*) sources [from Liu, W. et al. 2008a].

We now examine the spectral evolution of the LT source and defer that of the FP sources to §5.4.1. As shown in Figure 5.5*a*, the measured temperatures are consistent with a monotonic decrease with time, presumably due to cooling of the thermal plasma through various channels whose rate exceeds the heating rate at these times. The EM (Fig. 5.5*b*), on the other hand, increases rapidly in the first ∼5 minutes and then stays roughly constant followed by a slight decrease toward the end. The increase and decrease of the EM is likely due to chromospheric evaporation (e.g., Liu, W. et al., 2006) and/or direct coronal heating and consequent cooling of the plasma.

[2]The trend of the two FP spectra (being nearly parallel to one another) extends below 50 keV to ∼20 keV, suggesting that pulse pileup may have minimal effects on the relative spectral shapes of the FPs, and that our selection of 50 keV as the lower limit for reliable FP spectra is likely to be unnecessarily conservative.

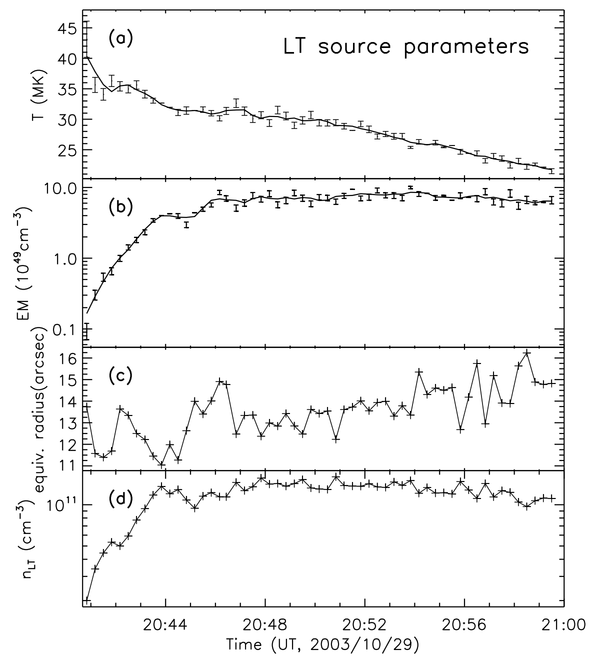

Figure 5.5: Evolution of spectroscopic parameters of the LT source. (*a*) Temperature T and (*b*) emission measure EM with 20 s integration time. The solid lines are 7-point box-car smooths of the original fitting results indicated by the symbols. (*c*) Radius r of the equivalent sphere of the LT source (see §5.2.2) and (*d*) corresponding electron number density $n_{\rm LT}$ [from Liu, W. et al. 2008a].

In order to infer the density of the LT source, we assumed that it has a spherical shape with the projected area a equal to the area inside the 50% brightness contour at 12–25 keV. We then obtained the radius $r = (a/\pi)^{1/2}$ and volume $V = 4\pi r^3/3$ of the *equivalent sphere* and the corresponding density $n_{\rm LT} = [{\rm EM}/(Vf)]^{1/2}$. In doing so we assumed a filling factor f of unity, and used the EM values smoothed with a 7-point box-car to minimize fluctuations possibly caused by the inevitable anti-correlation between T and EM during spectral fitting. The values of r and $n_{\rm LT}$ as functions of time are shown in Figures 5.5*c* and 5.5*d*, respectively. As evident, the size of the sphere stays roughly constant between $11''$–$16''$ and thus the density follows the same trend as the EM.

To obtain the spatial evolution of the double FP sources and the corresponding LT source, one can track the migration of their centroid positions with time. For each 12–25 and 60–100 keV image obtained in §5.2.1, we used contours at 50% and 90% of the maximum brightness of each LT and conjugate FP source, respectively, to locate its emission centroid. The reason for a higher contour level for the FPs (than the LT) is that the E-FP source spreads along the flare ribbon (see, e.g., Fig. 5.2*e*) and we need the brightest "kernel" to obtain the corresponding magnetic field strength averaged inside this contour (see §5.4.3). The resulting centroids at different times are superimposed on the multiwavelength images in Figure 5.6, and shown in greater detail in Figure 5.7, which we will examine in §5.3.

5.2.3 Multiwavelength Images

The following multiwavelength images were used in this analysis: magnetograms, Hα, white-light, and extreme ultraviolet (EUV). They were shifted by various amounts in the solar east-west (x) and south-north (y) directions to match the *RHESSI* aspect, believed to be accurate at the sub-arcsecond level (Fivian et al., 2002). All images were corrected for various geometric effects (solar rotation, *SOHO* L1 to Earth view, etc.) where applicable. These procedures are detailed in Appendix B.1.

A preflare *SOHO* MDI magnetogram at 20:30:35 UT is shown in Figure 5.6*a*, overlaid with the centroids of the *RHESSI* FPs at 60–100 keV obtained in §5.2.2 at 57 time intervals. E-FP is located in the negative (*dark*) polarity to the left of the general magnetic neutral line (*dashed*), while W-FP is in the positive (*white*) polarity to the right.

An Hα blue wing (6562.41 Å) image at 20:42:11 UT (Fig. 5.6*b*) displays flare ribbons in opposite magnetic polarities (cf., Fig. 5.6*a*). A *RHESSI* 60–100 keV image at the nearest time of 20:42:00–20:42:20 UT is overlaid as contours, which appear as three HXR sources on or near the three Hα kernels.[3] The strongest HXR FP source (E-FP) is cospatial with the brightest Hα emission that is located in the negative magnetic polarity, suggestive of the causal correlation between the flux of HXR-producing electrons and the heating rate of the lower atmosphere responsible for the Hα emission.[4] Note that E-FP is also associated with the major compact seismic signature, as reported by Donea & Lindsey (2005).

Comparing a *TRACE* white-light image at 20:49:49 UT shown in Figure 5.6*c* with Figure 5.6*a*, we find three large sunspots in the positive polarity to the right and three small sunspots in the negative polarity just left of the general neutral line. *RHESSI* 60–100 keV contours nearest in time are shown in gray,[5] where the double FP sources correspond to parts of the white-light flare emission (*light-gray contours* and *arrows*).

The *TRACE* 195 Å image at 20:50:42 UT in Figure 5.6*d* shows an arcade of flare loops distributed along the magnetic neutral line. Overlaid are *RHESSI* images at 12–25 keV for the LT sources and 60–100 keV for the FP sources at 20:50:40–20:51:00 UT. The former appear at the apexes of the EUV loops and the latter at the footpoints.

5.3 Two-phase Unshearing Motions of HXR Footpoints

We now examine in greater detail the motions of the HXR sources in the context of the multiwavelength observations described above. In an attempt to correct for projection effects and to obtain the true 3D loop geometry, we assumed that the centroids of the LT and two FP sources at a given time are connected by a semi-circular model loop. We then used the solar x and y coordinates of these three points in the sky plane to determine the

[3]The most south-west Hα kernel does not have a HXR counterpart, possibly due to *RHESSI*'s limited dynamic range ($\gtrsim$10:1).

[4]The weaker HXR W-FP is ahead (to the west) of the corresponding Hα kernel, which may result from direct (other than collisional) heating, or from cooling of the hot plasma previously heated by nonthermal electrons with an increasing emission measure, since Hα emission is sensitive to temperature and density. It is possible that our coalignment of the *RHESSI* and Hα images is not perfect, and the HXR image can be shifted to the left by a few arcseconds such that both E- and W-FP can lead their corresponding Hα kernels.

[5]Some weak HXR emission also appears between the two FPs, which is, most likely, an artifact caused by pulse pileup of the LT emission (see §A.4.2).

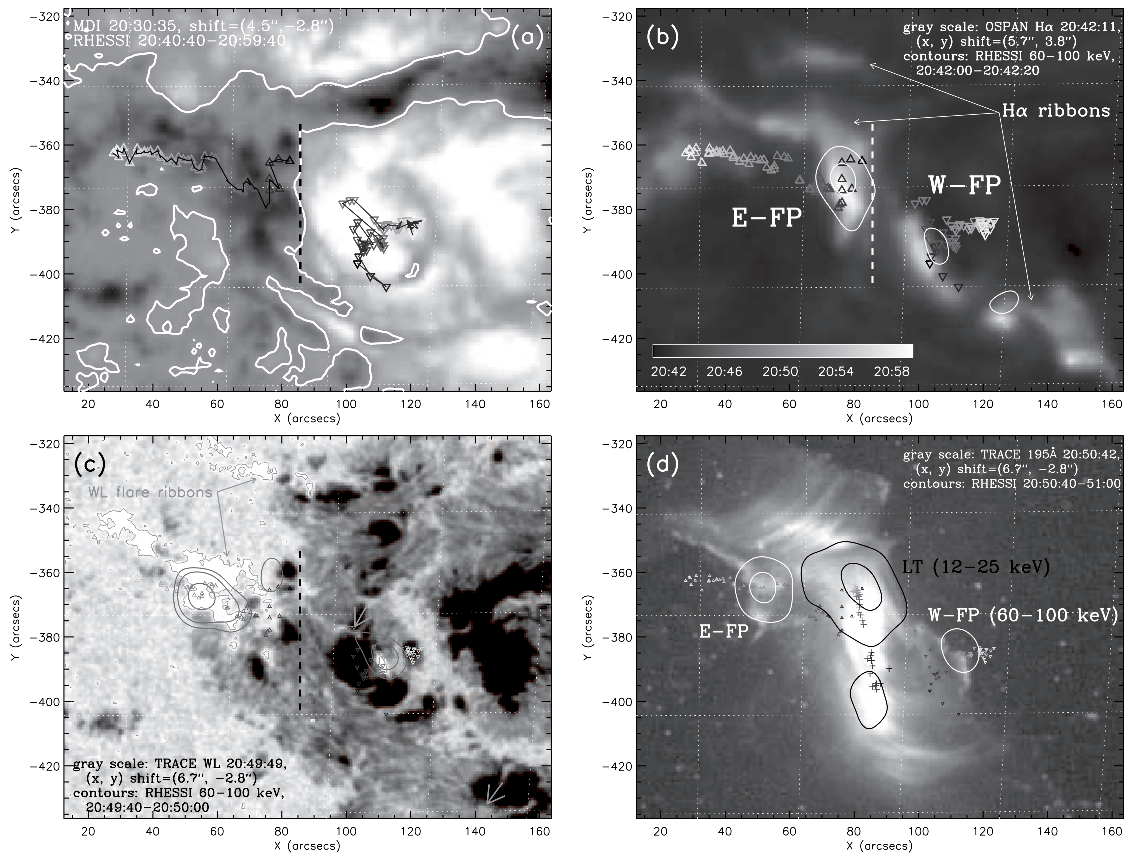

Figure 5.6: (a) preflare *SOHO* MDI magnetogram (centered at 20:30:35 UT with an integration time of 30 s) overlaid with magnetic neutral lines in white and *RHESSI* FP centroids as symbols. The white (dark) gray scale represents positive (negative) line-of-sight magnetic fields pointing away (toward) the observer. The vertical thick dashed line outlines the general magnetic neutral line between the two FPs, which is also shown in (b) and (c). The temporal evolution of the *RHESSI* centroid positions is indicated by the color bar in (b). Both the MDI magnetogram and *RHESSI* centroids were corrected for the solar differential rotation and shifted to their corresponding positions at the time of the *TRACE* image in (d); additional shifts of $\Delta x = 4.5'' \pm 2.0''$ and $\Delta y = -2.8'' \pm 2.0''$ were applied to the MDI map to compensate its pointing offset from *RHESSI* (see Appendix B.1). The same correction procedures were applied to (b), (c), and (d). (b) Same as (a) but for the Optical Solar Patrol Network (OSPAN) Hα blue wing (6562.41 Å) image taken at 20:42:11 UT showing the flare ribbons, overlaid with a concurrent *RHESSI* 60–100 keV image as gray contours (20% & 70%). (c) Same as (b) but for a *TRACE* white-light image at 20:49:49 UT and a *RHESSI* 60–100 keV image at contour levels of 20%, 30%, and 70%. The light-gray contours are at 99% of the maximum brightness of the *TRACE* image, highlighting some of the excessive white-light emission on the flare ribbons, the rest of which is marked by the two short arrows. (d) Same as (b) but for a *TRACE* 195 Å image at 20:50:42 UT, overlaid with concurrent *RHESSI* contours in dark (30% & 80%) for the LTs at 12–25 keV and in white (20% & 70%) for the FPs at 60–100 keV. The evolution of the LT (*plus signs*) and FP (*triangles*) centroids is also shown (see also Fig.5.7a) [from Liu, W. et al. 2008a].

size and the orientation of the semi-circle in 3D space, knowing that the FPs are located on the solar surface and the LT in the corona. A sample of the loops at selected times is shown in Figure 5.7*a*. We find that the inclination angle between the model loop and the solar surface ranges from 27° to 76°, and that the loop length ($l_{\rm total}$; see Fig. 5.7*c*) generally first decreases and then increases with a minimum at 20:43:50 UT.

The LT centroids (*plus signs*), as shown in Figure 5.7*a*, are situated at all times close to the neutral line (*dashed*) as expected, and form two clusters, one in the south and the other in the north. As time proceeds, the LT centroid appears to move from the apex of one loop to another along the arcade seen in *TRACE* 195 Å (Fig. 5.6*d*). It first gradually moves southward until 20:43:30 UT (marked by the open circle in Fig. 5.7*a*), when it starts to rapidly shift to the northern cluster and continue moving northward afterwards. This can be more clearly seen from its relative displacement projected onto the direction parallel to the north-south neutral line as a function of time shown in Figure 5.7*d* (Δy_{LT}, *dot-dashed line*).

As to the FPs, in general, E-FP first moves southward and then turns to the east, while W-FP first moves northward and then turns to the west, as indicated by two of the three thick arrows in Figure 5.7*a*. The evolution of the position of E-FP relative to W-FP (or the positional vector from W-FP to E-FP) is shown in Figure 5.7*b*. There is clearly a turning point which occurs at t_1=20:44 UT and divides the evolution of the FP positions into two phases: (1) Phase I (20:40:40–20:44:00 UT) when the two FPs generally move toward each other in a direction essentially parallel to the neutral line, (2) Phase II (20:44:00–20:59:40 UT) when the two move away from each other mainly perpendicular to the neutral line. The transition between the two phases coincides (within 30 s) with the minimum of the estimated loop length and the direction reversal of the LT motion noted above. Another signature of this two-phase division is the morphological transition at 20:43:20 UT, before which there are multiple FP sources, but only two FPs present afterwards (see Fig. 5.2). Below we describe in detail the HXR source evolution in the two phases.

We further decomposed the distance between the FPs into two components: perpendicular and parallel to the neutral line as shown in Figure 5.7*e*, where the two phases are divided by the vertical dotted line at t_1. As can be seen, the parallel distance (*asterisks*) first rapidly decreases at a velocity of 108 ± 18 km s^{-1} given by the linear fit during Phase I (covering a range of 27″ in ∼3 minutes); it then stays almost constant during Phase II with a slight increase (a range of 15″ in ∼16 minutes with 7 ± 1 km s^{-1}). In contrast, the perpendicular distance (*dashed*) has a small variation in Phase I (a range of 12″ with 15 ± 13 km s^{-1}) and increases continuously at a velocity of 51 ± 1 km s^{-1} in Phase II (range: 63″).

Next we obtained the shear angle (θ; Fig. 5.7*b*) from the normal to the neutral line (parallel to the y-axis) to the W-to-E relative positional vector, which is shown as a function of time in Figure 5.7*e* (*solid line*, *right axis*). This angle exhibits a fast decrease (from 56° to 22°) during Phase I and a slow decrease (down to 12°) during Phase II. An independent study by Ji et al. (2008) also found the same unshearing motions in two phases, which they referred to as *sigmoid* and *arcade* phases based on the X-ray morphology.

The unshearing motions of the HXR FPs indicate that the newly reconnected magnetic field lines are progressively less sheared during the flare. It can be seen that *TRACE* 195 Å loops corresponding to the HXR FPs at early times (not shown) are indeed highly sheared.

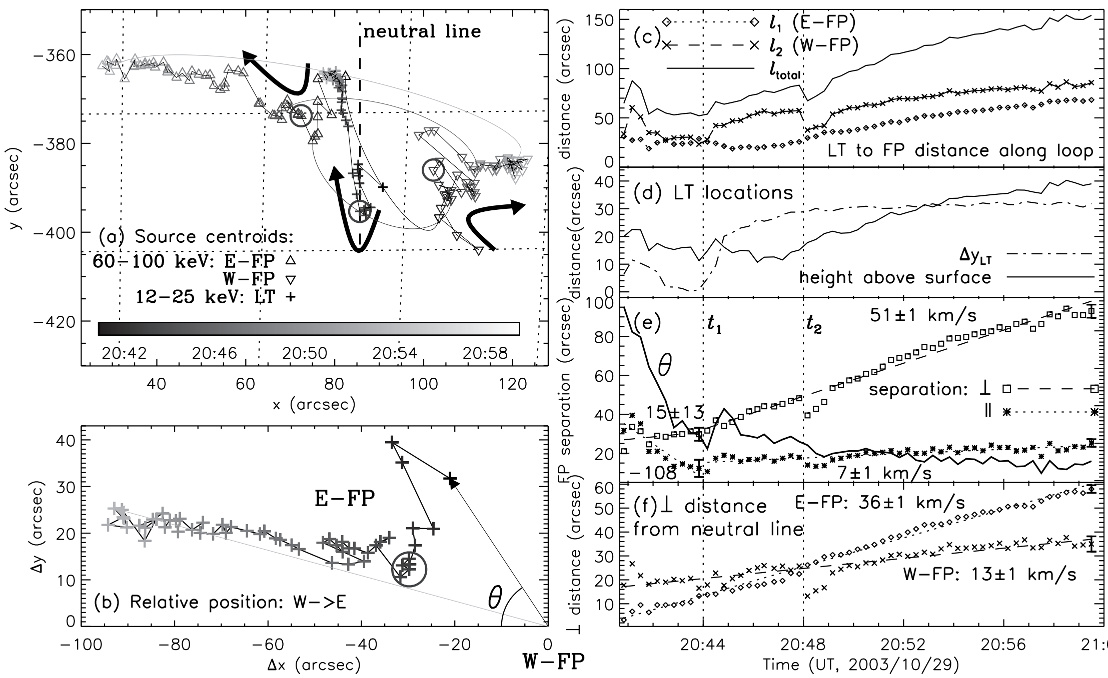

Figure 5.7: (*a*) Evolution of *RHESSI* centroids of the two FP sources at 60–100 keV (*triangles*) and of the LT source at 12–25 keV (*plus signs*), which are identical to those shown in Fig. 5.6*d*. Gray scales from dark to bright represent time at 20 s intervals from 20:40:40 to 20:59:40 UT. The vertical dashed line ($\parallel$ y-axis) is the general magnetic neutral line shown in Fig. 5.6*a*. We show semi-circular model loops at four times (labeled *a*, *d*, *f*, and *i* in Fig. 5.2) projected onto the sky plane, each of which connects three centroids (of two FPs & one LT) of the same time. The thick dark arrows indicate the general direction of motion for the LT and two FPs. (*b*) Relative centroid positions of E-FP with respect to W-FP which is selected as the origin. The start and end of the time evolution are marked by the black and light-gray arrows, respectively drawn from W-FP. θ is the shear angle between the normal (due west) to the neutral line and the line joining the two FP centroids. The circle here and those in (*a*) and the first vertical dotted line in (*e*) mark the transitional time t_1 from fast to slow unshearing motions of the FPs (see §5.3). (*c*) Distance (l_1 and l_2) from the LT centroid to the centroids of the two FPs along the semi-circular model loop as shown in (*a*), together with the length of the loop ($l_{\rm total} = l_1 + l_2$). The vertical dotted line labeled t_2 corresponds to the division between the two HXR peaks and the jump of the FP positions. (*d*) Relative displacement ($\Delta y_{\rm LT}$, *dot-dashed*) of the LT centroid parallel to the magnetic neutral line shown in (*a*) and estimated height of the LT centroid above the solar surface (*solid*). (*e*) Orthogonal components of the separation between W-FP and E-FP perpendicular (*squares*) and parallel (*asterisks*) to the neutral line. The straight lines are linear fits to the distances in the two phases, labeled with the corresponding velocities (in $\rm km\,s^{-1}$). The solid curve (*right scale*) is the shear angle θ defined in (*b*). (*f*) Perpendicular distances to the neutral line from E-FP (*diamonds*) and W-FP (*crosses*). Linear fits for the whole flare duration are shown as the straight lines. The error bar shown on the last data point of each line here and in (*e*) is the RMS deviation of the data from the corresponding fit [from Liu, W. et al. 2008a].

Similar unshearing motions were found in other flares in HXRs (Sakao, 1994; Masuda et al., 2001; Schmahl et al., 2006) and in EUV (Asai et al., 2003; Su et al., 2007). Note that the HXR flux (see Fig. 5.1) rapidly rises when the shear angle undergoes the fast decrease. An opposite process took place prior to the flare, that is, strong photospheric shearing flows observed near the neutral line (Yang et al., 2004, as mentioned earlier). This process increased the shear of field lines and built up magnetic stress and free energy in the system during the preflare phase (Metcalf et al., 2005).

It has been established for LT sources in limb flares that there is usually a decrease in altitude during the rising portion of the impulsive phase followed by a subsequent increase (e.g, Sui & Holman, 2003; Sui et al., 2004; Liu, W. et al., 2004a, 2008b). Holman et al. (2005) found 58 (66%) such events in a sample of 88 limb flares. For flares on the solar disk like the one under study, it is difficult to determine the LT height, but FP motions can be seen more clearly than those in limb flares. Our approach of determining a 3D semi-circle from the LT and FP centroids is an attempt to correct for projection effects and yields an estimate of the LT height as shown in Figure 5.7*d* (*solid line*).[6] As expected, the LT descent is evident especially before t_1=20:44 UT when the HXR flux is on the rise. It is associated with the southward motion of the LT along the neutral line before t_1 (Fig. 5.7*d*; *dot-dashed*). This suggests that the propagation of the reconnection site along the neutral line or the arcade in one direction and then the other temporally coincides with the decrease and then increaseof the LT altitude. The LT descent here is also associated in time with the decrease of the loop length (Fig. 5.7*c*, *solid line*) and the fast unshearing motion of the FPs (Fig. 5.7*e*, *solid line*), that is, with progressively shorter and less sheared loops. This association was previously proposed, based on a simple energy analysis, by Ji et al. (2007). They argued that an alternative interpretation for descending LTs that invokes the relaxation of cusp-shaped loops, however, cannot explain the approaching FPs which are expected otherwise not to move.

5.4 Temporal Correlations of Conjugate Footpoints

We now examine the temporal evolution of and correlations between various quantities of the two conjugate FPs, particularly spectral, spatial, and magnetic field parameters, which are summarized in Table 5.1.

5.4.1 Spectral Correlations

Figure 5.8*a* shows the history of the photon fluxes of E-FP (I_1, *diamonds*) and W-FP (I_2, *crosses*) at 50 keV obtained from the power-law fits in the 50–150 keV range mentioned in §5.2.2. We find that the two fluxes follow each other closely in their temporal trends and E-FP is always brighter than W-FP except for the first time interval. The correlation of the fluxes can also be seen in Figure 5.9*a* where one flux is plotted vs. the other. A linear regression is shown as the thick dashed line and given in Table 5.1. The correlation coefficients listed in Table 5.1 indicate a very high correlation in either a linear or a nonlinear sense. Such a correlation is expected for conjugate HXR FPs, since they are believed to be

[6] The slightly different temporal trends of the LT height and the loop length shown in Fig. 5.7*c* are due to the assumption that the semi-circle is not necessarily vertical to the solar surface.

Table 5.1: Correlation coefficients and linear regressions between various parameters of the conjugate footpoints for the full flare duration (20:40:40–20:59:40 UT).

Subscripts: 1: E-FP, 2: W-FP		r_p	No. of $\sigma(0.13)$	r_s	signif-icance	Linear regression (between quantities in first two columns)
I_1	I_2	0.98	8	0.97	10^{-35}	$I_2 = (-0.3 \pm 0.1) + (0.41 \pm 0.01)I_1$
γ_1	γ_2	0.90	7	0.89	10^{-20}	$\gamma_2 = (-0.5 \pm 0.3) + (1.17 \pm 0.07)\gamma_1$
B_1	B_2	0.39	3	0.40	10^{-3}	$B_2 = (-5.1 \pm 0.3) + (2.89 \pm 0.06)B_1$
B_1	$\log_{10} I_1$	0.50	4	0.49	10^{-4}	$I_1 = (0.014 \pm 0.002) \times 10^{(0.53 \pm 0.01)B_1}$
B_2	$\log_{10} I_2$	0.82	6	0.84	10^{-16}	$I_2 = (0.124 \pm 0.004) \times 10^{(0.150 \pm 0.001)B_2}$
$\bar{B}$	$\log_{10} \bar{I}$	0.77	6	0.84	10^{-16}	$\bar{I} = (0.140 \pm 0.007) \times 10^{(0.219 \pm 0.003)\bar{B}}$
v_1	v_2	0.63	5	0.29	10^{-2}	$v_2 = (-93 \pm 10) + (2.8 \pm 0.1)v_1$

r_p and No. of σ: Pearson's linear correlation coefficient and its multiple of 1σ uncertainty of $1/(57)^{1/2} = 0.13$, where 57 is the number of data points (time intervals), respectively;
r_s and significance: Spearman's rank correlation coefficient and significance level, respectively;
I (photons s^{-1} cm^{-2} keV^{-1}): HXR flux at 50 keV;
γ: spectral index between 50 and 150 keV (regression done only for 20:40:40–20:52:40 UT);
B (100 Gauss): magnetic field;
$\bar{B}$ (100 Gauss) and $\bar{I}$ (photons s^{-1} cm^{-2} keV^{-1}): B and I averaged between E-FP and W-FP;
v (km s^{-1}): FP velocity.

produced by similar populations of nonthermal electrons that escape the same acceleration region (believed to be at/near the LT source; Petrosian & Liu 2004; Liu, W. et al. 2008b) and travel down opposite legs of the same magnetic loop to reach the chromosphere.

We show the corresponding power-law indexes (γ) of the two FPs vs. time in Figure 5.8*d* and one index vs. the other in Figure 5.9*b*. Again we find that the two indexes are closely correlated, as can be seen from the large correlation coefficients (Table 5.1). The E-FP spectrum, however, is slightly harder than the W-FP spectrum, which it is persistent most of the time. The results from long integration intervals (2–3 minutes), which have better count statistics, exhibit the same pattern. We averaged the index values of the first six long intervals up to 20:52:40 UT, after which the uncertainties become large due to low count rates. This average gives $\langle\gamma_1\rangle = 3.63 \pm 0.06$ for E-FP and $\langle\gamma_2\rangle = 3.79 \pm 0.11$ for W-FP. Their difference of $\langle\gamma_2\rangle - \langle\gamma_1\rangle = 0.15 \pm 0.13$ is marginally significant at the 1σ level.

Let us compare the HXR fluxes and spectral indexes of the two FPs. As can be seen in Figures 5.8*a* and 5.8*d*, during HXR Peak 1 (before t_2=20:48 UT), the fluxes and indexes are anti-correlated, i.e., they follow the general "soft-hard-soft" (SHS) trend observed in many other flares (e.g., Grigis & Benz, 2004). However, during Peak 2 (after t_2), the indexes decrease through the HXR maximum and then vary only slightly (with relatively large uncertainties) around a constant level of 3.0. This trend can be characterized as "soft-hard-hard" (SHH). This flux-index relationship can also be seen in Figure 5.9*c* where the index averaged between the two FPs is plotted against the average flux. Note that the spectral index values during the late declining phase of the flare are even smaller than those at the maximum of the main HXR Peak 1. In this sense, the overall spectral variation can be characterized as "soft-hard-soft-harder". As we noted earlier, there were energetic protons detected in interplanetary space by *GOES* and *ACE* following the flare. These observations, when taken together, are consistent with the conclusion of the statistical study by Kiplinger

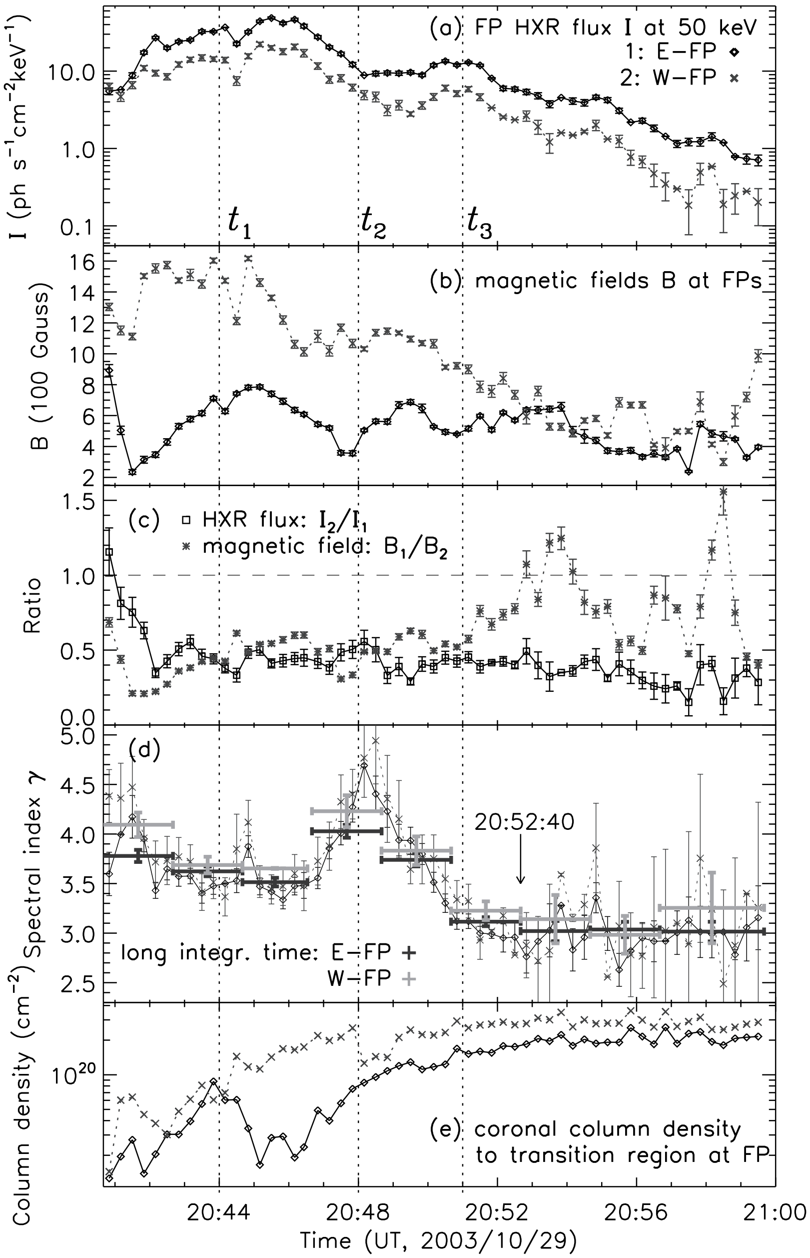

Figure 5.8: History of HXR and magnetic field parameters of the two footpoints. (a) HXR fluxes at 50 keV of E-FP (*diamonds*) and W-FP (*crosses*) obtained from power-law fits in the 50–150 keV range. The same symbol convention for E- and W-FP holds for the other panels. The vertical dotted lines correspond to the transitional times of t_1 and t_2 as shown in Fig. 5.1, and t_3, the maximum of HXR Peak 2. (b) *SOHO* MDI magnetic field strengths registered at the two FPs, with the $\pm\sigma$ uncertainties derived from 10 preflare magnetograms (see §5.4.3). (c) Ratios of the 50 keV fluxes (W-to-E) and magnetic fields (E-to-W) of the two FPs. (d) HXR spectral indexes of the two FPs from the same fits as in (a). The plus signs show results of long integration intervals (2–3 minutes) indicated by the wide horizontal error bars, which yield better count statistics. The arrow marks the end of the first six such intervals for averaging the index values (see §5.4.1). (e) Estimated coronal column densities from the edge of the LT source to the transition region at the two FPs [from Liu, W. et al. 2008a].

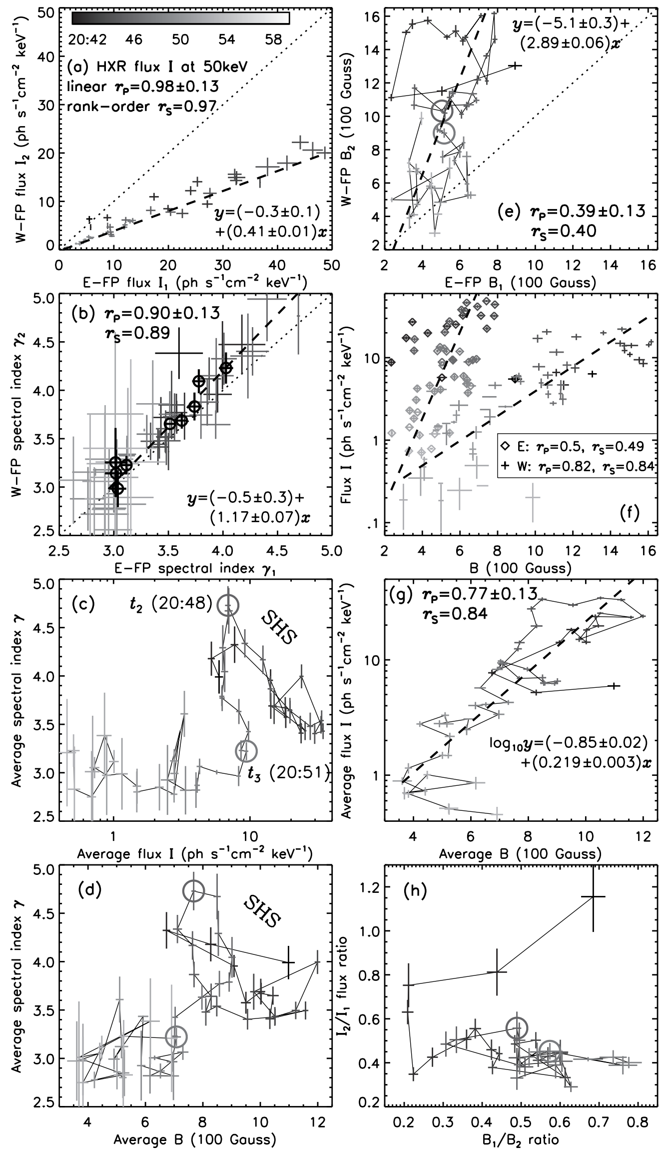

Figure 5.9: Various correlations between the HXR and magnetic field parameters of the two FPs. (a) HXR flux at 50 keV (Fig. 5.8a) of W-FP vs. E-FP with a linear regression fit (*dashed*). Pearson's linear and Spearman's rank-order correlation coefficients, r_p and r_s, are given in the legend. The color bar indicates the common time evolution for all panels of this figure. (b) Same as (a) but for the spectral indexes (γ) shown in Fig. 5.8d. The open circles represent the results obtained from longer integration intervals (2–3 minutes). The linear regression is done for the data points up to 20:52:40 UT. (c) and (d) Average (between the two FPs) spectral index $\bar{\gamma}$ vs. average flux $\bar{I}$ at 50 keV and vs. average magnetic field $\bar{B}$, respectively. The two open circles here and in (e) and (h) mark the times t_2 and t_3 shown in Fig. 5.8. Early in the flare, an usual "soft-hard-soft" (SHS) variation is present. (e) Same as (a) but for the magnetic field strengths of the two FPs as shown in Fig. 5.8b. (f) Logarithmic HXR flux at 50 keV vs. the corresponding magnetic field strength for E-FP (*diamonds*) and W-FP (*plus signs*). A general linear correlation is found for each FP, which translates to an exponential dependence of the HXR flux on the field strength. (g) Same as (f) but for the average values. (h) W-to-E HXR flux ratio vs. E-to-W magnetic field ratio of the two FPs as shown in Fig. 5.8c. A positive correlation is present only in the early stage of the flare [from Liu, W. et al. 2008a].

(1995) that this type of flare with progressive spectral hardening tends to be associated with SEP events (also see Saldanha et al., 2008). As we also noted, strong gamma-ray line emission was detected during this flare (Hurford et al., 2006), which indicates a significantly large population of accelerated protons at the Sun, but the relation to the SEPs at 1 AU is unclear.

5.4.2 Spatial Correlations

We now switch from the spectral characteristics of the two FPs to their spatial evolution. In §5.3 we focused on their relative motion, while here we examine their individual motions.

Figure 5.7*f* shows the perpendicular distance of each FP from the north-south neutral line (*dashed*, Fig. 5.7*a*) as a function of time. Linear fits of the full flare duration indicate mean velocities of $\langle v_\perp \rangle = 36 \pm 1$ and $13 \pm 1\,\mathrm{km\ s^{-1}}$ for E- and W-FP, respectively. These velocities are similar to those found by Xu et al. (2004) for white-light ribbons and by Krucker et al. (2005) for HXR FPs in this event. We also calculated the total velocities of the FP centroids i.e., $v = (v_\perp^2 + v_\parallel^2)^{1/2}$, where $v_\perp$ and $v_\parallel$ are the components perpendicular and parallel to the neutral line, respectively. The two resulting velocities have a linear temporal correlation at a 5σ level (see Table 5.1), which again provides evidence of the causal connection between the two conjugate FPs. However, the individual component, $v_\perp$ or $v_\parallel$, alone does not exhibit any noticeable correlation between the two FPs.

Figure 5.7*c* shows the distances from the LT centroid to the centroids of E-FP (l_1, *diamonds*) and W-FP (l_2, *crosses*) along the model semi-circular loop (see Fig. 5.7*a* and text in §5.3) as a function of time. Each curve follows the same general increase as the corresponding distance from the neutral line shown in Figure 5.7*f*.[7] We estimated the coronal column densities from the LT source to the transition region at the two FPs (see Appendix B.3 for details), $N_{\mathrm{tr},\,i} = 0.5 n_{\mathrm{LT}}(l_i - r)$, (where i=1, 2), using the distances l_1 and l_2 and the LT density n_{LT} and equivalent radius r obtained in §5.2.2 (Fig. 5.5). The results in Figure 5.8*e* show that there is a large relative difference from 20:44 to 20:48 UT during HXR Peak 1 but a smaller difference during Peak 2. Implications of these different column densities will be addressed in §5.5.2 and §5.5.3.

5.4.3 Magnetic Field Correlation

The magnetic field strengths of the two FPs were obtained from *SOHO* MDI magnetograms (e.g., see Fig. 5.6*a*) through the following steps: (1) We first selected a preflare[8] magnetogram at 08:30:35 UT and coaligned it with the *RHESSI* pointing and field of view (see Appendix B.1 for details). (2) For each time interval, the 90% brightness contour of each

[7]We note that the lines in Fig. 5.7*f* cross each other at ∼20:48 UT with that of E-FP increasing faster, while the lines in Fig. 5.7*c* increase at about the same rate with that of W-FP always being larger (apart from only one time interval). This is because the distances plotted in Fig. 5.7*f* are measured on the sky plane, while the distances in Fig. 5.7*c* are evaluated along the semi-circle in 3D space, which corrects for projection effects. Since the flare occurred in the western hemisphere, the distance of W-FP to the neutral line is a more significant underestimate of its true 3D distance to the LT than that of E-FP.

[8]Note that magnetograms during the flare cannot be used because measurements of magnetic fields in the flare kernels are not reliable (see Appendix B.1). However, photospheric magnetic fields usually show minimal changes or virtually no changes at all before and after a flare. This justifies our approach of using the preflare field to approximate the field during the flare.

RHESSI FP source was rotated back to the corresponding position at the time of the MDI map to account for the solar rotation. Then the MDI pixels enclosed in this contour were averaged to give a value of the magnetic field for this FP. (3) The above two steps were repeated for each of the ten MDI magnetograms recorded between 20:25 and 20:35 UT at a one minute cadence (excluding the one at 20:28 UT that are contaminated by artificial pixel spikes). The average of the ten independent measurements is used as the final result for the magnetic field (Fig. 5.8*b*) and the standard deviation gives the plotted uncertainty, which is on the order of a few percent, comparable to the nominal MDI noise of 20 G (Scherrer et al., 1995).

Figure 5.8*b* shows the history of the resulting magnetic field strengths. The field strength of W-FP generally decreases with time, while that of E-FP fluctuates about its mean value. Most of the time (especially before t_3=20:51 UT), the W-FP field (positive polarity) is stronger than the E-FP field (negative polarity), while their fractional difference generally decreases as time proceeds. The temporal variations of the two field strengths are only weakly correlated (again, particularly before t_3) at the 3σ level (see Table 5.1), as can also be seen in Figure 5.9*e*.

5.4.4 Inter-correlations Among Spectral, Spatial, and Magnetic Field Parameters

We are now ready to examine the relationship between the HXR fluxes and the magnetic fields of the two conjugate FPs. We plot the logarithmic HXR flux vs. the magnetic field strength for each FP in Figure 5.9*f*. As we can see here and noted before, E-FP (*diamonds*) has a larger flux and a weaker magnetic field, while W-FP (*plus signs*) has a smaller flux and a stronger magnetic field. In addition, the flux is correlated with the field strength for each FP (see Table 5.1 for the correlation coefficients and linear regressions). The logarithmic average flux ($\bar{I}$) and magnetic field ($\bar{B}$) of the two FPs are shown one vs. the other in Figure 5.9*g*. A linear relationship, as shown by the thick dashed line with a correlation coefficient of $r_p = 0.77\pm0.13$, is clearly present. In other words, $\bar{I}$ is exponentially (*nonlinearly*) correlated with $\bar{B}$, the expression of which is listed in Table 5.1. We also plot the average spectral index ($\bar{\gamma}$) vs. $\bar{B}$ in Figure 5.9*d*. Since $\bar{I}$ is correlated with $\bar{B}$, the "soft-hard-soft" type of relationship between $\bar{\gamma}$ and $\bar{I}$ translates to that between $\bar{\gamma}$ and $\bar{B}$. Namely, $\bar{\gamma}$ is anti-correlated with $\bar{B}$ during the early phase of the flare (before t_3=20:51 UT).

We now check the relationship of the spatial evolution and magnetic field variation of the two FPs. As noted in §5.4.2, E-FP moves faster than W-FP away from (perpendicular to) the magnetic neutral line. We also note that, (1) $B\langle v_\perp \rangle$ is proportional to the magnetic reconnection rate, and (2) E-FP (W-FP) is located in a weaker (stronger) magnetic field. This anti-correlation of the velocity and magnetic field strength means that, as expected, about the same amount of magnetic flux is annihilated from each side of the neutral line. However, the magnetic fluxes swept by the two FPs, $\int B\langle v_\perp \rangle dt$ integrated over the full flare duration, differ by 44% of their average value. This is not expected, but Fletcher & Hudson (2001) also reported such unbalanced magnetic fluxes for the 2000 July 14 flare. One explanation could be that the flare ribbons, which, when taken as a whole, may yield balanced fluxes, whereas the HXR FPs, which cover only parts of the ribbons, do not.

There are interesting relationships between the HXR FP positions and the magnetic topology. The trajectory of E-FP is located in or next to a narrow channel of a strong negative magnetic field (see Fig. 5.6*a*), and its early portions are next to the three small sunspots just east of the neutral line (Fig. 5.6*c*). Meanwhile, W-FP runs through the umbra of a large sunspot where there is a strong positive magnetic field. Liu et al. (2007) found that these two HXR FPs were *adjacent* to two patches of positive current helicity that disappeared after the flare. It is also possible that the FPs were located at the *edges* of strong vertical currents, similar to the situation found by Canfield et al. (1993). In particularly, for E-FP alone, McTiernan et al. (2004) found that it moved along a morphological separatrix, based on a force-free extrapolation of the Mees vector magnetograms.

5.4.5 Implications of Various Correlations

The correlation (Fig. 5.9*g*) between the average HXR flux ($\bar{I}$) and the average magnetic field ($\bar{B}$) reveals important information about the magnetic reconnection and particle acceleration processes. Here we suggest two alternative interpretations that are consistent with the observations.

1. The *nonlinear* (exponential) nature of the $\bar{I}$-$\bar{B}$ correlation indicates that particle acceleration is very sensitive to the magnetic field strength. In the stochastic acceleration model of Petrosian & Liu (2004), this can be interpreted from the following aspects: (1) The level of turbulence is proportional to δB^2 (where δB is the magnetic field amplitude of plasma waves), which is proportional to the wave energy density and determines the number of the accelerated electrons. When the magnetic field strength B increases, δB is likely to increase as well and so does the flux of accelerated electrons. (2) The acceleration rate is proportional to $B(\delta B/B)^2$, which determines the spectral hardness of the electron distribution. When B increases, if $\delta B/B$ remains constant or even decreases but at a lower rate, the acceleration rate will increase and result in a harder electron spectrum. (3) In addition, the model predicts that the relative efficiency of acceleration of electrons, and thus their spectral hardness increase with decreasing values of the ratio of electron plasma frequency to gyrofrequency, $\alpha \equiv \omega_{pe}/\Omega_e \propto 1/B$. These theoretical arguments are qualitatively consistent with the observations that the magnetic field strength is correlated with the HXR flux and anti-correlated with the spectral index. Here we have assumed that the photospheric magnetic field strengths measured at the FPs are scaled with the field strength in the coronal reconnection region, measurements of which are difficult and unavailable.

2. Alternatively, noting that the velocities ($v_\perp$) of the two FPs perpendicular to the magnetic neutral line remain roughly constant during the flare (see Fig. 5.7*f*), the correlation between the average HXR flux and magnetic field strength simply translates into the correlation between the HXR production rate and the magnetic flux annihilation rate or reconnection rate, $Bv_\perp$. Furthermore, since $Bv_\perp$ is believed to be proportional to the electric field in the reconnection region (Forbes & Lin, 2000), it then follows that the particle acceleration rate correlates with the electric field. According to the DC electric field acceleration model (Holman, 1985; Benka & Holman, 1994), a larger electric field results in a larger high-energy cutoff ($E_{\max}$) for the electron spectrum. A higher value of $E_{\max}$ lead to a harder HXR spectrum below $E_{\max}$, if $E_{\max}$ is within one or two orders of magnitude at the observed photon energies (Holman, 2003). Therefore, the observed anti-correlation

between the magnetic field strength and spectral index may also be explained by the electric field acceleration mechanism, provided that $E_{\rm max}$ is not far above the energy range for fitting the photon spectrum. Note that Krucker et al. (2005) studied the motion of E-FP *alone* in this flare and found a rough temporal correlation between the HXR flux and reconnection rate, characterized by the product of Bv or B^2v, where v includes the velocity both perpendicular and parallel to the neutral line.

5.5 HXR Footpoint Asymmetries

As mentioned above and partly noted by Liu, W. et al. (2004b), Xu et al. (2004), and Krucker et al. (2005), the two conjugate FPs exhibit the following asymmetric characteristics: (1) the *brighter* E-FP is located in a *weaker*, negative magnetic field, while the *dimmer* W-FP is located in a *stronger*, positive field; (2) the two FPs have very similar spectral shapes with E-FP being slightly harder; (3) E-FP is located *closer* to the LT than W-FP; (4) E-FP moves *faster* away from the magnetic neutral line than W-F. These asymmetries are summarized in Table 5.2.

Table 5.2: Asymmetric characteristics of the conjugate footpoints (E-FP and W-FP): mean, median, and their E-to-W ratio of various quantities.

	Mean			Median		
	E	W	E/W	E	W	E/W
I	13.7	6.1	2.2	8.9	4.6	1.9
B	520	960	0.55	520	1010	0.51
γ	3.63	3.79	0.96	3.4	3.5	0.96
l	41	60	0.69	38	60	0.64
$N_{\rm tr}$	1.2	2.1	0.60	1.2	2.5	0.50
$v_\perp$	36	13	2.8	—	—	—

I (photons s^{-1} cm^{-2} keV^{-1}): HXR flux at 50 keV;
B (Gauss): magnetic field strength;
γ: spectral index between 50 and 150 keV;
l (arcsecs): distance from the LT centroid to the FP centroid along the semi-circular loop;
$N_{\rm tr}$ (10^{20} cm^{-2}): coronal column density from the edge of the LT source to the transition region at the FP.
$v_\perp$ (km s^{-1}) : velocity perpendicular to the neutral line;
The mean spectral indexes are the averages of the results of the first six long integration intervals before 20:52:40 (see §5.4.1), while all the other values listed here are from the results of the 57 short intervals throughout the flare.

We explore in this section different possibilities that can cause such asymmetries, particularly the asymmetric HXR fluxes and spectra. Various physical processes can contribute and they fall into two categories according to their origins: (1) asymmetry during particle acceleration, and (2) asymmetry arising from particle transport. The second category includes effects of magnetic mirroring and column density, which will be examined in what follows together with other transport effects (§5.5.1–5.5.4). The first category was historically thought to be less likely and will be discussed later in §5.5.5. We use both the flux ratio $R_I \equiv I_2/I_1$ and the asymmetry (c.f., Aschwanden et al., 1999) defined by Alexander

& Metcalf (2002):

$$A \equiv (I_1 - I_2)/(I_1 + I_2) = (1 - R_I)/(1 + R_I), \tag{5.1}$$

to quantify the asymmetric HXR fluxes, with $A = \pm 1$ being 100% asymmetry and $A = 0$ being perfect symmetry.

5.5.1 Magnetic Mirroring

Asymmetric magnetic mirroring is commonly cited to explain asymmetric HXR fluxes observed at conjugate FPs. We examine to what extent mirroring alone can explain the observations of this flare. For simplicity, we make the following assumptions for our analysis below: (1) Disregard all non-adiabatic effects of particle transport, i.e., energy losses and pitch-angle diffusion due to Coulomb collisions. By this assumption, the magnetic moment of a particle is conserved and mirroring is the only effect that changes the pitch angle when the particle travels in the loop and outside the acceleration region. (2) Assume an isotropic pitch-angle distribution of the electrons at all energies upon release from the acceleration region. (3) Disregard details of bremsstrahlung, and assume that the nonthermal HXR flux is proportional to the precipitating electron flux at the FP.[9]

The loss-cone angle for magnetic mirroring is given as

$$\theta_i = \arcsin \sqrt{B_0/B_i} \tag{5.2}$$

where i=1 for E-FP and 2 for W-FP, B_0 is the magnetic field strength at the injection site in the corona where particles escape from the acceleration region, and B_i is the field strength at the ith FP in the chromosphere. By the isotropy assumption, the fractional flux of the forward moving electrons that will *directly* precipitate to the chromosphere (whose pitch angle is located inside the loss cone) can be evaluated by integrating over the solid angle (also see, Alexander & Metcalf, 2002):

$$F_i = \frac{1}{2\pi} \int d\Omega = \frac{1}{2\pi} \int_0^{2\pi} d\phi \int_0^{\theta_i} \sin\theta d\theta = 1 - \mu_i \,, \tag{5.3}$$

where the pitch-angle cosine is $\mu_i = \cos\theta_i = (1 - B_0/B_i)^{1/2}$. If there is strong mirroring, i.e., $B_0 \ll B_i$, we have $\mu_i \simeq 1 - B_0/(2B_i)$, and if there is no mirroring, i.e., $B_0 = B_i$, we have $\mu_i = 1$. By our assumptions (1) and (3) above, such a fraction should be independent of electron energy and is proportional to the HXR flux I_i at the corresponding FP. It then follows that

$$R_I \equiv \frac{I_2}{I_1} = \frac{F_2}{F_1} = \frac{1-\mu_2}{1-\mu_1} \simeq \begin{cases} \frac{B_1}{B_2} \equiv R_B^{-1}, & \text{if } B_0 \ll B_i,\ (i = 1,\, 2), \\ \frac{B_1}{2B_2} \equiv R_B^{-1}/2, & \text{if } B_0 = B_1,\ B_0 \ll B_2, \end{cases} \tag{5.4}$$

the second case of which corresponds to the possibility that mirroring occurs only at one FP, but the required condition $B_1 \ll B_2$ does not apply to this flare. In either case, the HXR flux ratio should be correlated with the inverse of the magnetic field ratio, R_B^{-1}. This result is consistent with that of the strong diffusion case obtained by Melrose & White (1981).

[9] This flux includes the precipitation of electrons previously reflected by mirroring back to the acceleration region at the LT where they may be scattered and/or re-accelerated, presumably by turbulence.

As shown in Table 5.2, the mean/median HXR flux of E-FP is about twice that of W-FP, while the mean/median magnetic field strength of E-FP is about a factor of two smaller. This is consistent with the mirroring effect in the average sense of the whole flare duration. We can further see if this relationship also holds at different times. Figure 5.8*c* shows the W-to-E ratio ($R_I = I_2/I_1$) of the HXR fluxes and the E-to-W ratio ($R_B^{-1} = B_1/B_2$) of the field strengths of the two FPs as a function of time. We find a temporal correlation between the two ratios during the first $\sim$3 minutes when both first decrease and then increase. In the middle stage (20:43–20:51 UT) of the flare, both ratios remain roughly constant with marginal fluctuations and similar mean values of $\langle R_I \rangle = 0.43$ and $\langle R_B^{-1} \rangle = 0.50$. After 20:51 UT, the magnetic field ratio increases significantly with large fluctuations and exceeds unity in 6 of the 57 time intervals, while the flux ratio remains at about the same level as before. The same temporal evolution can also be seen in Figure 5.9*h* where the flux ratio is plotted against the magnetic field ratio. The behavior of the two ratios before 20:51 UT is expected from magnetic mirroring, but their significant difference after 20:51 UT cannot be explained by mirroring alone.

5.5.2 Column Density

Another transport effect that can cause asymmetric HXR FPs is different coronal column densities experienced by electrons in traveling from the acceleration region to the transition region at the two FPs (Emslie et al. 2003; Liu, W. 2006). The effective column density is $N_{\rm tr,\,eff} = N_{\rm tr}/\langle \mu \rangle$, where $\langle \mu \rangle$ is the average pitch angle cosine, and $N_{\rm tr} = \int_0^{s_{\rm tr}} n(s) ds$ is the coronal column density to the transition region at distance $s = s_{\rm tr}$ along the magnetic field line with $n(s)$ being the ambient electron number density. A difference in $\langle \mu \rangle$, $s_{\rm tr}$, and/or $n(s)$ between the two legs of the flare loop can lead to different effective column densities. (1) Different pitch-angle distributions can be caused by asymmetric magnetic mirroring and/or asymmetric acceleration. (2) Different path lengths $s_{\rm tr}$ can be caused by a magnetic reconnection site located away from the middle of the loop (Falewicz & Siarkowski, 2007). (3) Different densities $n(s)$ can also occur because magnetic reconnection takes place between field lines that are previously not connected and their associated densities are not necessarily the same. It takes time (on the order of the sound travel time, $\gtrsim$ tens of seconds) for the newly reconnected loop to reach a density equilibrium, but the observed HXRs could be produced before then.

Column density asymmetry affects the FP asymmetry in two ways, since both energy losses and pitch-angle scattering due to Coulomb collisions take place at about the same rate that is proportional to the column density: (1) Column density asymmetry is related to energy losses, bremsstrahlung, and the way we calculate the FP photon flux in §5.2.2 (integrating HXR photons primarily produced below the transition region). Electrons with an initial energy of E are stopped after traveling through a column density $N_{\rm stop}(\,{\rm cm}^{-2})/ \approx 10^{17}[E(\,{\rm keV})]^2$. If $N_{\rm stop}$ is smaller than or comparable to the column density to the transition region ($N_{\rm tr}$), in one half of the loop with a *larger* column density, there are *more* electrons stopped in the leg and thus less electrons reaching the transition region. This results in *more* HXRs produced in the leg and less HXRs beneath the transition region (counted as the FP flux), since bremsstrahlung is proportional to both column density and electron flux. (2) Different Coulomb scattering rates result from different column densities on the two sides of the loop, which can cause different pitch-angle distributions, even if the particles are injected with symmetrical pitch angles from the acceleration region.

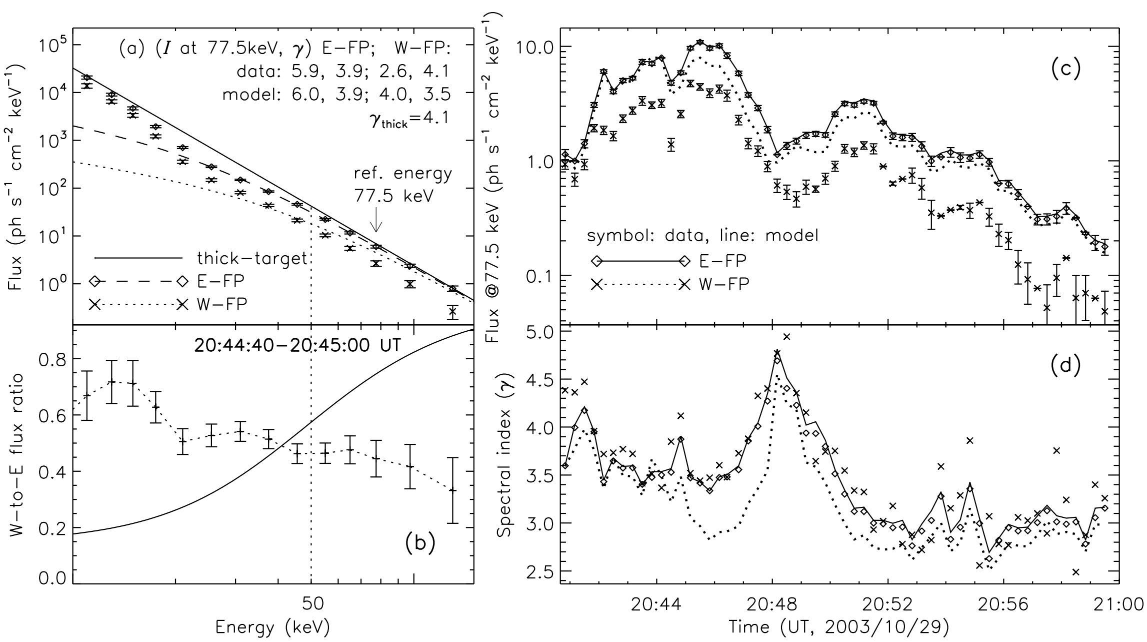

Figure 5.10: Effects of asymmetric coronal column densities. (*a*) Photon fluxes of E-FP (*diamonds*) and W-FP (*crosses*) vs. energy at 20:44:40–20:45:00 UT (same as Fig. 5.4*a*), superimposed with model fluxes (*lines*) evaluated below the transition region based on asymmetric coronal column densities using eq. (5.5). The solid line shows the power-law thick-target flux with an index of $\gamma_{\rm thick} = 4.1$. The legend shows the fluxes (I) at a reference energy of 77.5 keV (selected at the center of the middle energy bin above 50 keV) and the spectral indexes (γ) above 50 keV of the two FPs for both the data (from power-law fits to the 50–150 keV count rates) and model. (*b*) Ratio of the W-to-E FP fluxes shown in (*a*), with the plus signs and solid line from the data and model (given by eq. [B.5]), respectively. (*c*) Observed (*symbols*) and modeled (*lines*) fluxes of E- and W-FP at 77.5 keV vs. time (cf. Fig. 5.8*a* at 50 keV). (*d*) Same as (*c*) but for the spectral indexes above 50 keV. The data are the same as in Fig. 5.8*d* but plotted without error bars for clarity [from Liu, W. et al. 2008a].

Focusing on the energy dependence of FP HXR asymmetry, we present below an estimate of the column density effect *alone*, while assuming no magnetic mirroring and identical pitch-angle distributions (same $\langle\mu\rangle$) in the two loop legs. The relevant formulisms are derived in Appendix B.2. We assumed that identical power-law electron fluxes with a spectral index δ and the same pitch-angle distribution are injected into the two legs of the flare loop, which have the same ambient density but different path lengths $s_{\rm tr}$ to the FPs. Our goal is to examine if this scenario can yield photon fluxes and spectra consistent with observations for both FPs. For each of the 57 time intervals shown in Figure 5.8, we first used the E-FP column density N_{tr} (see §5.4.2 and Fig. 5.8*e*) from the edge of the LT source (assumed to be the acceleration region) to obtain its dimensionless form $\tau_{\rm tr} = N_{tr}/(5 \times 10^{22}\,{\rm cm}^{-2})$, which ranges from 5×10^{-4} to 1×10^{-2}. We then substituted $\tau_{\rm tr}$ into

$$I_{\rm FP}(\tau_{\rm tr}, k) = A_0 k^{-(\delta-1)} \left(1 + \tau_{\rm tr} \frac{k+1}{0.37k^2}\right)^{1-\delta/2} , \tag{5.5}$$

rewritten from equation (B.4), where A_0 is the normalization for the thick-target flux and k is the photon energy in units of the rest electron energy 511 keV. With this equation, we fitted the E-FP spectrum above 50 keV in a least-squares sense by iteratively adjusting the free parameters A_0 and δ. Using the resulting A_0 and δ and W-FP's $\tau_{\rm tr}$, we then calculated the W-FP spectrum by equation (5.5) and the W-to-E flux ratio by equation (B.5).

Figure 5.10*a* shows an example of the spectra of the two FPs and their model predictions, together with the corresponding thick-target spectrum produced by the same power-law electron flux. We only trust the observed FP spectra > 50keV, as noted earlier, due to pulse pileup. As expected, the model FP fluxes are reduced from the thick-target flux, especially at low energies, because low-energy electrons are more susceptible to collisional energy loss and pitch-angle scattering. This results in a spectral flattening (hardening)[10] in the FP X-ray spectrum. Because of its larger column density, the W-FP's model spectrum exhibits more flux reduction at a given energy and a flattening to a higher energy. Above 50 keV the model spectrum of the brighter E-FP fits the data very well. However, that of the dimmer W-FP does not fit the data at all, since the model flux is much greater (e.g., at 77.5 keV $I = 4.0$ vs. 2.6 photons s^{-1} cm^{-2} keV^{-1}) and harder ($\gamma = 3.5$ vs. 4.1) than the observed flux, and even harder than the E-FP flux ($\gamma = 3.5$ vs. 3.9). This can be best seen in Figure 5.10*b* that shows the data (*plus signs*) and model (*solid line*) ratios of the W-to-E FP flux. The data ratio generally decreases with energy or stays roughly constant above 50keV within uncertainties, but the model ratio is an increasing function of energy. These trends generally hold throughout the flare as can be seen from the history of HXR fluxes and spectral indexes shown in Figures 5.10*c* and 5.10*d*.

In summary, the model predicts a much harder photon spectrum for the dimmer W-FP with the larger coronal column density, while according to the observations the dimmer W-FP is as hard as or slightly softer than the brighter E-FP (see Fig. 5.10*d*). Saint-Hilaire et al. (2008) reported similar results that the majority of the brighter FPs in their 172 pairs of FPs tend to have harder spectra. In addition, the differences between the model HXR fluxes of the two FPs are too small to explain the observations (Fig. 5.10*c*). One may attempt to increase the difference between the column densities in order to increase the flux difference and thus to merge this gap between the model and data, but the discrepancy of the spectral indexes would be worse since the W-FP spectrum would be relatively even harder. Therefore, we conclude that the column density effect alone cannot provide a self-consistent explanation for the asymmetric HXR FPs observed here.

Our conclusion is different from that drawn by Falewicz & Siarkowski (2007), who found in three flares that the HXR flux ratios of asymmetric FPs were consistent (within a factor of 2) with the predictions from asymmetric column densities. While the column density scenario may apply to those flares, we should note the following facts that can lead to different conclusions, because their observations set less stringent constraints than our

[10] This FP spectral flattening should not be confused with the flattening of the spatially integrated spectra found by Sui et al. (2007).

RHESSI observations: (1) The analyses of Falewicz & Siarkowski (2007) were limited to images made by *Yohkoh* HXT *Yohkoh* in the M1 (23–33 keV) and M2 (33–55 keV) bands, while our observations cover a higher and wider energy range from 50 to 150 keV. The column density effect is more pronounced in the M1 and M2 bands than at higher energies (see Fig. 5.10*a*). Moreover, M1 images could be contaminated by thermal emission that can mislead their prediction based on a nonthermal bremsstrahlung model. (2) They did not obtain the model spectra of the FPs and compare them with the observations, as we did with multiple energy bins. This was enabled by *RHESSI*'s $\sim$1 keV resolution in the energy range of 3 to a few hundred keV, as opposed to HXT's four broad energy bands in the 14–93 keV range.

5.5.3 Magnetic Mirroring and Column Density Combined

We have seen from the above discussions that each of the two transport effects *alone* can only explain to some extent the observed FP asymmetries: (1) Asymmetric magnetic mirroring is consistent with the asymmetric HXR fluxes in the average sense of the flare duration, but it has difficulties in accounting for the flux asymmetry later in the flare. (2) Asymmetric column densities in the two legs of the flare loop are qualitatively consistent with the asymmetric HXR fluxes, but their quantitative predictions of fluxes and spectral hardness contradict the observations. These two transport effects, in reality, operate at the *same time*, because electrons experience Coulomb collisions while being mirrored back and forth in the loop, and thus the collisionless (adiabatic) assumption that we adopted earlier for simplicity for magnetic mirroring needs to be dropped. In particular, since W-FP has stronger mirroring (than E-FP), the average pitch angle of electrons impinging there is larger, and thus the effective column density $N_{\rm tr,\,eff} = N_{\rm tr}/\langle\mu\rangle$ is greater than previously thought. This can enhance the column density asymmetry. In what follows, we attempt to provide an explanation for some aspects of the observations by combining the two effects.

From the above discussion and the observations presented earlier (see §5.4), we should pay attention to the distinction between the two HXR peaks: As shown in Figure 5.8*c*, during Peak 1 (before t_2=20:48 UT) the FP HXR flux asymmetry seems to be mainly controlled by magnetic mirroring, because of the temporal correlation between the HXR flux ratio and the inverted magnetic field ratio. During Peak 2 (after t_2) magnetic mirroring seemingly fails to control the asymmetry because the correlation gradually disappears, especially after the HXR maximum at t_3=20:51 UT. A viable explanation for the two-peak distinction is that (1) at early times, the density (Fig. 5.5*d*) and length (Fig. 5.7*c*) of the loop are small, resulting in small coronal column densities (Fig. 5.8*e*) from the acceleration site to the FPs. Energy losses and pitch-angle scattering due to Coulomb collisions are less important, and therefore the rates of electron precipitation to the FPs are mainly governed by mirroring. (2) Later in the flare, as the density and loop length have increased considerably, the column densities become larger and the collisional effects become more important than before in shaping the observed FP flux asymmetry. In addition, since magnetic mirroring depends on the gradient $d \ln B/dN$ (e.g., Leach & Petrosian, 1981), this effect becomes less important when the column density N increases faster than the relative change of magnetic field from the LT to the FP, which is possibly the case later in the flare. Therefore, at later times, the prediction of magnetic mirroring alone tends to deviate from the data, which might be explained by the two transport effects combined. Unfortunately, we cannot offer a quantitative prediction about the outcome of the combination without detailed modeling, which is briefly discussed in §5.6 as future work.

There are several coincidences with the two-peak division which seem to have causal connections: (1) As noted in §5.4.1, the correlation between the HXR fluxes and spectral indexes (Figs. 5.8*a* and 5.8*d*) can be described as common "soft-hard-soft" during Peak 1 and as "soft-hard-hard" during Peak 2. The spectral hardening at later times may be associated with the increase of the column density in the loop (Fig. 5.8*e*), due to collision-caused hardening mentioned above (§5.5.2). (2) During Peak 1, the magnetic fields at the two FPs correlate with each other (Fig. 5.8*b*), while this correlation becomes progressively vague during Peak 2, especially after its maximum t_3=20:51 UT, possibly because of longer loops. (3) The transition (t_2=20:48 UT) between the two HXR peaks coincides with the sudden jump in the positions of both FPs (Figs. 5.7*a* and 5.7*f*), the dip in the loop length (Fig. 5.7*c*), and the valley in the magnetic field strengths (Fig. 5.8*b*). This points to the start of the new episode of energy release of Peak 2, presumably associated with a new series of loops that have physical conditions different from those in Peak 1. This transition may be related to the different behaviors of magnetic mirroring during the two peaks noted above.

5.5.4 Other Transport Effects and FP Asymmetries

Here we briefly discuss transport effects other than magnetic mirroring and column density that can contribute to the observed HXR flux and spectral asymmetries. Some of these effects compete with one another, which may explain why the spectral index difference is so small ($\langle\gamma_2\rangle - \langle\gamma_1\rangle = 0.15 \pm 0.13$).

1. **Non-uniform target ionization** along the path of high-energy electrons was ignored in the above analysis as we assumed fully ionized plasma in the background. However, in the 10^4–10^5 K chromosphere and transition region, the material is only partially ionized. The presence of neutral atoms reduces the rates of long-range collisional energy losses and pitch-angle scattering and thus increases the bremsstrahlung efficiency (Brown, 1973b; Leach & Petrosian, 1981; Kontar et al., 2002). For a power-law electron flux injected to a model of targets varying from fully ionized in the corona to neutral in the chromosphere, the high energy HXR flux can be elevated by a factor of 2.8 from that with fully ionized targets (Brown, 1973b). The photon spectral index has the usual relationship $\gamma = \delta - 1$ at low ($\lesssim$10–20 keV) and high ($\gtrsim$100–200 keV) energies, but in the intermediate energy range the index is smaller (flatter) by as much as $\sim$0.5. The energy E_* at the downward knee of the spectral hardness transition depends on the column density to the transition region, with $E_* \propto (N_{\rm tr})^{1/2}$ (Kontar et al., 2002). For the flare under study, electrons can penetrate deeper into the chromosphere and thus encounter more neutral atoms at the E-FP with weaker magnetic mirroring, while stronger mirroring at W-FP stops more electrons in the fully ionized corona. Equivalently, as we mentioned before, the effective column density to the transition region $N_{\rm tr,\,eff}$ and thus E_* are larger at W-FP because of larger average pitch angles. This results in a higher HXR flux and harder spectrum in the 50–150 keV range at E-FP than at W-FP, which qualitatively agrees with the observations.

2. **Relativistic beaming and photospheric albedo** associated with different pitch-angle distributions also play a role. At E-FP with weaker mirroring, the angular distribution of electrons are more concentrated to the forward direction down to the photosphere than at W-FP. The forward relativistic beaming effect of radiation is an increasing function of electron and thus photon energy. While the FPs are seen on the solar disk from above, we therefore expect to observe less high-energy photons emitted upward at E-FP (McTiernan & Petrosian, 1991), which would result in a softer spectrum there. In the meantime, since more photons are (beamed) emitted downward at E-FP, photospheric albedo or Compton back-scattering (Langer & Petrosian, 1977; Bai & Ramaty, 1978) is stronger there than at W-FP. Because the effect of albedo is basically moving photons from high to low energies, stronger albedo also leads to a softer spectrum at E-FP. Relativistic beaming and albedo are pronounced mainly at relativistic ($\gtrsim$MeV) and low ($\lesssim$40 keV) energies, respectively, but they may have residual effects in the 50–150 keV range. The spectral softening of these two effects competes with the hardening caused by other effects mentioned above (column densities and non-uniformly ionized targets), which may eventually lead to the observed similar spectral indexes of the two FPs.

3. **Return currents** are another possible origin of FP HXR asymmetry. The electric field associated with the return current decreases the energy of the downward-streaming electrons, with the major impact being on the lower-energy electrons (Zharkova & Gordovskyy, 2006). The result is a low-energy cutoff in the electron distribution, qualitatively similar to that produced by Coulomb collisions. Different precipitating electron beam fluxes in the two legs of the flare loop will induce different return current densities and associated electric field strengths, and thus result in different HXR fluxes and spectral shapes at the two FPs. However, asymmetric magnetic mirroring may or may not cause different electron beam fluxes, because the larger total number of precipitating electrons at the brighter E-FP with the weaker magnetic field may be canceled out by the larger cross-sectional area of that leg (due to conservation of the magnetic flux). Without an accurate measurement of the loop cross-sections, it is difficult to assess the effects of return currents on the FP HXR asymmetries in this flare.

5.5.5 Acceleration-induced Asymmetry

We address here the first category of explanations for FP HXR flux asymmetry that is related to intrinsic asymmetry or anisotropy arising from the particle acceleration process.

1. Acceleration-produced intrinsic anisotropy and its energy dependence are influenced by the following factors: (1) In the HXR producing energy range, ten to several hundred keV, the rate of scattering of electrons by *turbulence or plasma waves* increases with energy (see Fig. 11 in Petrosian & Liu, 2004). (2) On the other hand, as mentioned earlier, the pitch-angle scattering rate due to *Coulomb collisions* is a decreasing function of the electron energy. If we assume that the acceleration process produces some initial anisotropy (e.g., the pancake shaped pitch-angle distributions found by Minoshima et al., 2008) at all energies, a combination of these two effects will result in electrons at intermediate energies being better able to preserve their initial anisotropy, while higher and lower energy electrons are isotropized by waves and Coulomb collisions, respectively.

If we further neglect other asymmetry-causing effects, and if the initial anisotropy means

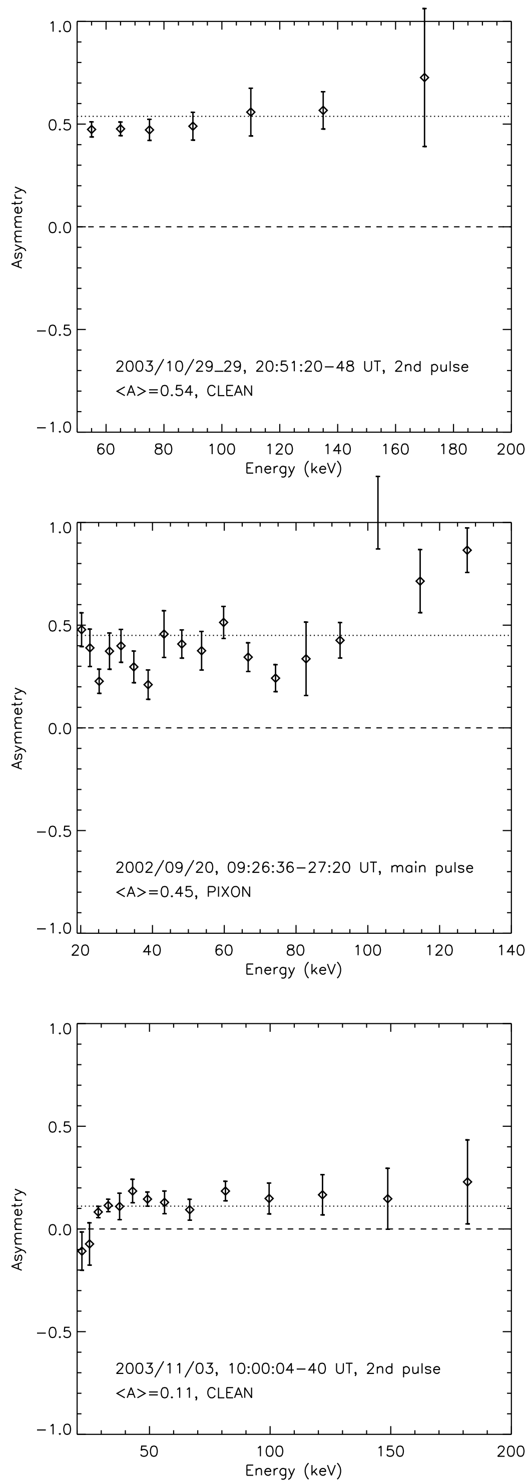

Figure 5.11: FP flux asymmetry vs. energy for the 2003-10-29 X10 flare (*top left*) and other events. The dotted line marks the mean value and the dashed line marks zero (perfect symmetry).

more electrons moving in *one* direction along the magnetic loop, the above outcome translates into a larger HXR flux asymmetry $|A|$ (see eq. [5.1]) at intermediate photon energies and a smaller asymmetry at higher and lower energies. This was found by Alexander & Metcalf (2002) in a flare whose maximum asymmetry $|A|_{\max}$ occurs in the energy range of 20–40 keV. McClements & Alexander (2005) attributed this to an asymmetric, energy-dependent injection in which more electrons are injected preferentially into one leg of the loop rather than into the other. Zharkova & Gordovskyy (2004) also found that in a reconnection current sheet the electric field can produce asymmetric electron and proton beams.

For the X10 flare under study here, however, it is difficult to check asymmetry in the low to intermediate energy range (below 50 keV) because of strong pileup effects as noted before. Above 50 keV, asymmetry either increases with energy (see the flux ratio in Fig. 5.4*b*) or remains constant, which is opposite to the decreasing asymmetry found by Alexander & Metcalf (2002) in this energy range. In addition, our initial analysis of several other flares of different *GOES* classes found no indication of a universal or general energy-dependent pattern of FP HXR flux asymmetry (see Fig. 5.11), which is consistent with that found by Aschwanden et al. (1999) from *Yohkoh* HXT *Yohkoh* data. Furthermore, in the stochastic acceleration model, it is difficult to realize in the turbulence region an asymmetric particle accelerator that can send significantly more particles to one side than to the other. Whether the scenario described above and proposed by McClements & Alexander (2005) is the rule or an exception remains an open question.

2. As one possible mechanism, *some* electrons might be accelerated locally by waves near/at the FPs, as suggested by Liu, W. et al. (2006) based on *RHESSI* observations and by Fletcher & Hudson (2008) based on theoretical arguments. On the one hand, this scenario could contribute to FP asymmetries in various ways; on the other hand, it has difficulties such as in accelerating particles in the dense chromosphere and in explaining the observed time-of-flight energy dependencies (Aschwanden et al., 1995).

5.6 Summary and Discussion

We have presented imaging and spectral analysis of the *RHESSI* observations of the 2003 October 29 X10 flare showing two conjugate HXR footpoints (FPs), which are well-defined during the bulk of the flare duration. One FP lies to the east (E-FP) and the other to the west (W-FP) of the north-south magnetic neutral line. This flare provides a unique opportunity to study in great detail the spatial, temporal, and spectral properties of the FPs and their associated magnetic fields. The impulsive phase was relatively long ($\sim$20 minutes), HXR fluxes were detected by *RHESSI* at energies up to hundreds of keV, and it was located close to disk center, resulting in minimum projection effects and excellent magnetic field measurements from *SOHO* MDI. Our main findings regarding the unshearing motions, various correlations, and asymmetric characteristics of the two FPs are as follows.

1. **Two-phase unshearing motions** are present in the flare: In Phase I the two identified FPs become closer to each other as they rapidly move almost parallel to the magnetic neutral line. In Phase II the FPs move away from each other more slowly, mainly perpendicular to the neutral line (Fig. 5.7*a*). In other words, the shear angle θ between the normal to the neutral line and the line connecting the two FPs exhibits a fast and then slow decrease from 56° to 12° (Fig. 5.7*e*). This indicates that the newly reconnected magnetic

field lines are progressively less sheared (closer to a potential field), which is consistent with the results of Ji et al. (2008). In addition, the transition between the two phases of the FP motions coincides with the direction reversal of the apparent motion of the loop-top (LT) source along the neutral line (Fig. 5.7*d*, *dot-dashed*), and the minima of the estimated loop length (Fig. 5.7*c*, *solid line*) and LT height (Fig. 5.7*d*, *solid line*). This suggests that the *initial decrease* of the LT altitude observed in many other *RHESSI* flares (e.g., Sui & Holman, 2003; Sui et al., 2004; Liu, W. et al., 2004a, 2008b) may be associated with progressively shorter loops during the *fast unshearing* motion phase when the reconnection site propagates along the arcade. The subsequent increase of the LT altitude could be due to reconnection occurring in progressively longer and higher loops.

2. There are **correlations** among the temporal evolutions of various quantities (Table 5.1). Some of them exhibit distinct differences between the two HXR peaks (transition at 20:48 UT): (*a*) The HXR fluxes (Figs. 5.8*a* and 5.9*a*) and spectral indexes (Figs. 5.8*c* and 5.9*b*) of the two FPs are strongly correlated. This is strong evidence that the two HXR sources are from conjugate FPs at the two ends of the same magnetic loop. (*b*) The HXR flux and spectral index of each FP show a commonly observed "soft-hard-soft" evolution (Figs. 5.8*a*, 5.8*d*, and 5.9*c*) during HXR Peak 1, while during Peak 2 the spectrum becomes harder and stays hard even as the HXR flux decays. This event falls into the statistical category (Kiplinger, 1995) of the association of progressive flare spectral hardening with SEPs. (*c*) The magnetic field strengths at the two FPs also exhibit some temporal correlation (Figs. 5.8*b* and 5.9*e*) particularly during Peak 1. This is further evidence that the selected FPs are conjugate. (*d*) The FP HXR flux exponentially correlates with the magnetic field strength (Figs. 5.9*f* and 5.9*g*). There is also an anti-correlation between the average spectral index and magnetic field strength during Peak 1 (Fig. 5.9*d*). These correlations suggest that stronger magnetic fields, and/or larger reconnection rates or larger electric fields in the reconnection region are responsible for producing larger fluxes and harder spectra for the accelerated electrons and thus the resulting HXRs. This is in qualitative agreement with the predictions of the stochastic acceleration model (Petrosian & Liu, 2004) and the DC electric field acceleration model (Holman, 1985). In particular, the exponential nature of the correlation means that particle acceleration is very sensitive to the magnetic field strength, which is consistent with the prediction of the stochastic acceleration model that electrons are preferentially accelerated in strongly magnetized plasma.

3. Various **asymmetries** are observed between the conjugate FPs (Table 5.2): (*a*) On average, the eastern footpoint (E-FP) HXR flux is 2.2 times higher than that of the western footpoint (W-FP; Fig. 5.8*a*), while its magnetic field strength is 1.8 times weaker (520 G vs. 960 G; Fig. 5.8*b*). This is consistent with asymmetric magnetic mirroring that predicts a smaller HXR flux at the FP with the stronger magnetic field (§5.5.1). (*b*) Both FPs move away from the magnetic neutral line at roughly constant velocities, but the brighter E-FP moves 2.8 times faster in the weaker magnetic field than does the dimmer W-FP in the stronger field ($\langle v \rangle = 36 \pm 1$ vs $13 \pm 1\,\mathrm{km\,s^{-1}}$; Fig. 5.7*f*). This means that roughly equal amounts of magnetic fluxes from both polarities are being annihilated during reconnection. (*c*) The average estimated coronal column density from the edge of the LT source (assumed to be the acceleration region) to the transition region at E-FP is 1.7 times smaller than that of W-FP (1.2×10^{20} vs. $2.1 \times 10^{20}\,\mathrm{cm^{-2}}$; Fig. 5.8*e*). This qualitatively agrees with the HXR flux asymmetry, because a larger coronal column density results in

more HXRs produced in the loop legs and thus less HXRs emitted from the FP below the transition region, especially at low energies (Fig. 5.10; §5.5.2). (*d*) The photon spectra above 50 keV of the two FPs are almost parallel to each other (Fig. 5.4*a*), with the brighter E-FP being consistently slightly harder than the dimmer W-FP (Fig. 5.8*d*). Their mean index values $\langle\gamma_1\rangle = 3.63 \pm 0.06$ and $\langle\gamma_2\rangle = 3.79 \pm 0.11$ have a marginal difference of $\langle\gamma_2\rangle - \langle\gamma_1\rangle = 0.15 \pm 0.13$. In other words, the W-to-E ratio of the photon fluxes is a constant or a slightly decreasing function of energy. This contradicts the column density effect which would produce a much harder spectrum at the dimmer W-FP (Fig. 5.10). (*e*) As expected from asymmetric magnetic mirroring, there is a temporal correlation between the W-to-E HXR flux ratio and the E-to-W magnetic field ratio. However, this correlation only holds during HXR Peak 1 but gradually breaks down during Peak 2 (Figs. 5.8*c* and 5.9*h*). We suggest that a combination of the asymmetric magnetic mirroring and column density effects could explain this variation (§5.5.3). This is because as the column densities in the loop increase with time (Fig. 5.8*e*), collisions become more important, making the HXR flux ratio deviate from the prediction of mirroring alone. The increased column densities, possibly together with magnetic trapping, may also contribute to the observed spectral hardening later during the flare mentioned above. (*f*) Other *transport* effects including non-uniform target ionization, relativistic beaming, and photospheric albedo in the presence of different pitch-angle distributions caused by asymmetric mirroring, and/or return current losses, may also play a role in determining the relative HXR fluxes and spectral shapes of the conjugate FPs (§5.5.4). It is unclear whether there is observational evidence of asymmetry produced in the particle *acceleration* process (§5.5.5).

In our analysis we have treated the magnetic mirroring and column density effects separately in order to make the problem analytically tractable, yet without loss of the essential physics. However, in reality, the two effects are coupled and they should be studied together self-consistently to obtain a quantitative model prediction. This is done with the Fokker-Planck particle transport model of Leach & Petrosian (1981) in a converging magnetic field geometry. Results from such an analysis will be published in the future. In addition to numerical modeling, we have started a statistical study of *RHESSI* flares showing double FP sources that are close to disk center and thus have less projection effects. We hope to conduct future joint observations with *RHESSI*, *Hinode*, and the *Solar Dynamic Observatory* (*SDO*) to obtain more advanced measurements of the magnetic fields at FPs. These future investigations will help improve our understanding of the underlying physics of asymmetric HXR FPs.